Article

CFD Investigation of a Hybrid Wells Turbine with Passive Flow Control

Mohammad Nasim Uddin [1] **, Michael Atkinson** [1,*] **and Frimpong Opoku** [2]

1   Department of Mechanical Engineering, North Carolina A&T State University, Greensboro, NC 27411, USA
2   Senior Structural Engineer, Collins Aerospace, 190 Oak Plaza Blvd, Winston-Salem, NC 27105, USA
*   Correspondence: mdatkinson@ncat.edu

Abstract: In the past decade, there has been renewed interest in wave energy harvesting utilizing oscillating water columns (OWC), one of the most well-studied wave energy harnessing technologies. In the OWC, pneumatic power from ocean waves is converted to mechanical energy by Wells turbines. It should be noted, however, that such turbines tend to perform poorly, have a limited operating range, and have low efficiency. In the present study, we incorporate a rectangular Gurney flap (GF) at the trailing edge (TE) of a Wells turbine consisting of hybrid airfoil (NACA 0015 and NACA 0025) blades with variable chord distribution along the span. This passive flow control mechanism was adopted to achieve increased power production by the Wells turbine. This study aimed to determine the aerodynamic performance of the variable chord turbine with GF compared to a turbine with a constant chord. By using ANSYS™ CFX, the three-dimensional, steady-state, incompressible Reynolds averaged Navier–Stokes (RANS) equations coupled with the k-ω SST turbulence model are solved. The performance was evaluated through the use of non-dimensional coefficients of torque, pressure drop, and efficiency. In addition, the numerical accuracy was achieved through a grid independence study. There was a good agreement between the computed results and the available experimental and numerical data. The GF increased the torque coefficient by 18.6% and 47.3% but with the expense of peak efficiency of 8.5% and 7.4% for the baseline and the hybrid turbine, respectively. Additionally, the hybrid turbine with GF delayed the onset of the stall by ~3° angle of attack (AOA).

Keywords: wave energy; Wells turbine; Gurney flap; CFD; RANS; turbulence; blade stall

1. Introduction

Renewable energy sources are becoming increasingly popular among global leaders and policymakers due to the depletion of fossil fuels and awareness of their environmental impact. In addition to providing a clean and eco-friendly alternative to fossil fuels, ocean wave energy can significantly increase the electricity supply worldwide. In addition, wave energy offers many advantages, such as high energy density, minimal environmental impact, and low energy loss, even when waves travel long distances [1]. According to recent studies, ocean waves produce approximately 30,000 TWh of energy annually, sufficient for meeting the global demand for electricity if harnessed effectively [2].

Wave energy converters (WECs) play a critical role in commercializing wave energy [3]. The development of WECs and related technologies have been studied extensively over the past few decades. Owing to their simplicity, the most practical wave energy devices are based on the principle of OWCs. The OWC generates mechanical energy using an air turbine. High-speed turbine rotors produce electricity when paired with a generator.

When the wave oscillates, the air trapped on the free water surface in an OWC compresses and expands. Consequently, the OWC system is subject to unsteady bi-directional airflow, which requires particular types of turbines.

Professor Wells proposed the Wells turbine, commonly used by OWC WECs. It features a high rotational speed, a robust design, and high reliability [4]. Several symmetrical airfoil

blades are arranged at 90° staggered angles around the Wells turbine rotor hub. (Figure 1) The direction of tangential force acting on the blades is not affected by the flow direction when the blades are oriented symmetrically, as shown in Figure 2. Thus, it produces unidirectional torque independent of the direction of airflow.

The Wells turbine, however, has some inherent limitations, including a limited range of operation, low aerodynamic efficiency, increased noise levels, and poorer starting characteristics relative to other turbine types (e.g., impulse turbines). This has led to several authors' attempts at improving the Wells turbine designs.

In order to determine the aerodynamic performance of different design modifications, researchers have conducted experimental and numerical investigations. For example, the experiments by Curran and Gato [5] and Gato et al. [6] evaluated several possible design approaches.

An experimental study by Thakker et al. [7] examined the effect of guide vane shape on the turbine's performance, finding that the 3D guide vane improved efficiency by 4.5%. However, the downstream guide vanes play a significant role in reducing turbine efficiency since downstream guide vanes were responsible for about 21% of the average pressure loss, as reported experimentally [8].

Watterson et al. [9] found that the turbine performance drops with the increase in tip clearance. The effect of various uniform tip clearances under steady flow conditions was investigated by comparing numerical and experimental results [10]. In terms of turbine efficiency, it has been concluded that as the tip clearance to chord length ratio increases, the peak efficiency decreases, and shifts to a higher flow coefficient while the stall margin widens. With the aid of an endplate, tip leakage flow can be adjusted in order to improve the efficiency and range of operation [11,12]. Researchers [13,14] have also implemented neural network algorithms [15,16] to control the airflow and improve the Wells turbine stalling performance.

The introduction of blade sweep and skew reduced losses, delayed stalls, and minimized drag forces [17]. The experimental work [18] compares the aerodynamic performance of backward swept angle blades to unswept angle blades of different rotor solidities (0.64 and 0.32) at 0° and 20° pitch angles. In the 0° pitch setting, the swept back angle blade produces higher efficiency and torque value than the unswept blades, however, at the cost of peak efficiency.

In their work, Starzmann and Carolus et al. [4] investigated backward and forward sweep and the combination of the backward and forward sweep, i.e., backward at the hub and forward at the tip. According to the experimental investigation, neither a backward sweep nor a forward sweep alone increases efficiency and power or reduces the turbine's noise. However, it allows the operating range to be expanded by 106%. Therefore, they recommended a 15° backward sweep at the hub and a 5° forward sweep at the tip.

Little research has been conducted on introducing a Gurney flap (GF) to the Wells turbine's blade. However, using experimental data, Graham et al. [19] demonstrated that increasing GF height or reducing thickness increased lift significantly.

A rectangular flap (flap height = 1.5% C and flap width = 0.5% C) was implemented by Kotb et al. [20,21] to maximize the torque coefficient. Similarly, Kumar and Samad et al. [22] investigated different GF lengths and found that adding GF to the blades increased the output torque but reduced the turbine's efficiency due to the increased pressure drop.

Researchers [23] also investigated the effects of a circular cavity (CC) in a rectangular Gurney flap, cavity geometries, Gurney flap geometries, and Reynolds numbers on the Wells turbine performance. As compared with a conventional Wells turbine, a circular cavity within a rectangular Gurney flap achieved a 27.58% increase in average torque coefficient.

It is vitally important to determine the thickness of the airfoil because it significantly influences the aerodynamics, the stall point, and the weight of the turbine. For instance, thick airfoil blades are advantageous for improving the turbine's self-start ability [24,25].

Generally, a thick profile is preferable for small-scale turbines, while a thin profile is recommended for large-scale turbines [26].

Some researchers [27,28] recently examined entropy generation around the Wells turbine due to viscous dissipation. Comparing NACA0015 to other airfoils, it exhibits a lower global entropy generation rate and increased efficiency. However, an analysis of the performance of four different airfoils shows that NACA0015 is not the best under all conditions. For instance, NACA0012 gives a lower global entropy generation rate than NACA0015, and NACA0020 offers the smallest value. Therefore, when creating an optimum airfoil, a more efficient design than NACA0015 makes sense.

A typical Wells turbine with a constant chord length exhibits radial flow drift downstream of the rotor, causing the blades to stall at the tip rather than the hub at higher flow rates [1]. Torresi et al. [1] employed a variabledafs chord rotor to mitigate this phenomenon and found that several factors affect the turbine's efficiency; the relative velocity distribution along the blade's leading edge is of particular importance.

Bearing that in mind, to achieve constant linear growth from the hub to the tip, Soltanmohamadi et al. [29] proposed a variable chord rotor consisting of hybrid airfoil blades (NACA0012 & NACA0022) with a constant taper ratio of 1.58.
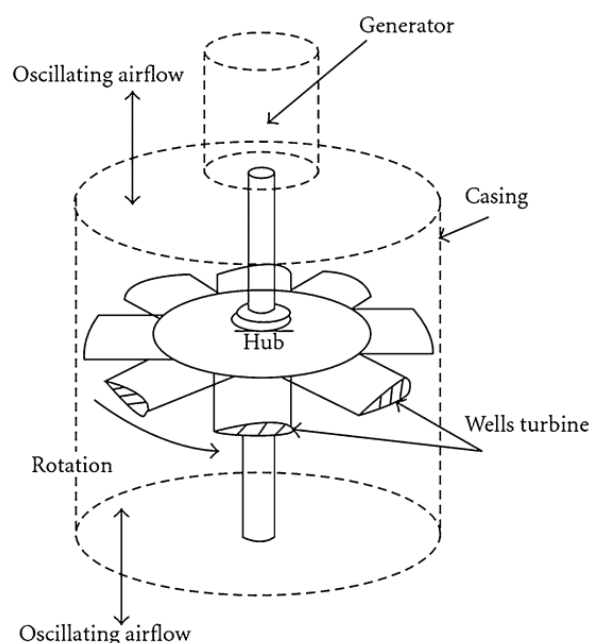

Figure 1. Schematic of a Wells turbine [29].

Suzuki and Arakawa et al. [30] investigated fan-shaped blades with (NACA0012 & NACA0021) airfoils with various sweep angles; the efficiency improved at an AOA < 7°. Takao et al. [31] investigated four different blade profiles, including NACA0020, NACA0015, CA9, and HSIM 15-262123-1576, and determined that the NACA0015 was the optimum rotor blade profile for the Wells turbine.

Takao and Okuhara et al. [32] studied three-dimensional blades (NACA0015 at the hub, NACA0020 at the mean radius, and NACA0025 at the tip) and compared them with two-dimensional (original) blades. The authors concluded that the three-dimensional blades improved efficiency and stall characteristics.

In the present study, we integrated a rectangular GF (Figure 3) into the TE of a Wells turbine consisting of hybrid airfoil (NACA 0015 and NACA 0025) blades with variable chord distribution along the span. The current work assessed the aerodynamic performance of the hybrid turbine with GF compared to a turbine with a constant chord. A thorough analysis of the complex flow field surrounding the turbine blades was also conducted. ANSYS[TM] CFX was used to solve the steady-state incompressible RANS equations in three dimensions. Throughout the study, the non-dimensional torque, efficiency, and pressure

drop have been used as performance parameters of the turbine. The accuracy of our numerical results was assured through a grid independence study [2,33–38]. Furthermore, the numerical model was validated by comparing the computed results to the available experimental data [5] and the results of other CFD investigations [39] covering a wide range of flow rates.
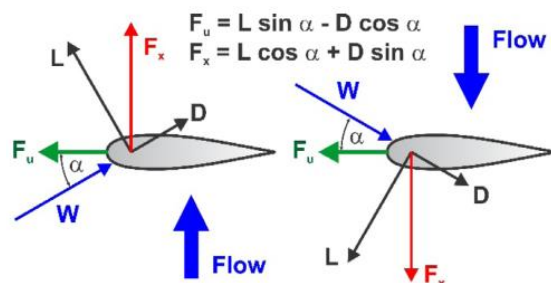

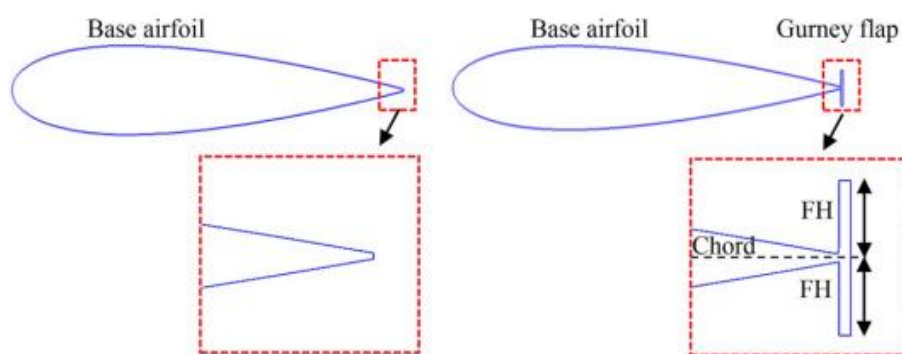**Figure 2.** Velocity triangles and force analysis of a Wells turbine [40].
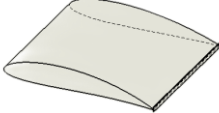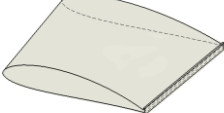

Figure 3. Baseline airfoil (**left**) and airfoil with Gurney flap on both sides (**right**) [22].

2. Materials and Methods

For this study, a Wells turbine with eight blades located perpendicular to the hub axis is chosen as the baseline geometry. The turbine blades comprised NACA 0015 symmetrical profiles oriented in a staggered pattern at 90 degrees. Detailed specifications are provided in Table 1 for the baseline turbine.

Table 1. Main features of turbine designs.

Parameters	Baseline	Baseline with GF	Hybrid with GF
no. of planes	1	1	1
no. of blades	8	8	8
chord length from hub to tip	125 mm	125 mm	79–125 mm
solidity at mean radius	0.67	0.67	0.67
Tip radius	300 mm	300 mm	300 mm
hub-to-tip ratio	0.67	0.67	0.67
tip clearance	1.25 mm	1.25 mm	1.25 mm
blade profiles from hub to tip	NACA 0015	NACA 0015	NACA 0025 to NACA 0015

WECs operate at a low airflow frequency (f = 1 Hz), producing negligible dynamic effects; it would be appropriate to use a steady-state solver [32]. Due to its ability to

accurately capture separation and adverse pressure gradients, an eddy-viscosity-based, two-equation k-ω SST turbulence closure model was chosen.

The equations are discretized using a fully implicit discretization method. The advection terms are discretized using a second-order scheme, while the diffusion terms are computed using a shape-function-based approach.

The velocity and pressure field of turbulent flows has two components: the fluctuating component and the mean component. Through the averaging of Navier–Stokes equations over time, RANS equations are derived. However, convective acceleration in the velocity field still produces fluctuations in the Navier–Stokes equations, although they are inherently nonlinear, as seen in Equation (1). As a result, we obtain the nonlinear term 'Reynolds stress', which Boussinesq identifies as a function of the mean flow components to solve the closure problem (Equation (2)).

$$
\underbrace{\nabla.(\rho UU)}_{Inertia\ Force} = - \underbrace{\nabla p}_{Pressure\ Force} + \underbrace{\rho g}_{Gravitational\ Force} +
$$

$$
\underbrace{\nabla.\left[\mu\left(\nabla U + (\nabla U)^{T}\right)\right] - \nabla\left(\frac{2}{3}\mu(\nabla.U)\right)}_{Viscous\ Force} - \underbrace{\nabla.(\overline{\rho U'U'})}_{Reynolds\ Stress} , \tag{1}
$$

$$
\underbrace{(\overline{\rho U'U'})}_{Reynolds\ Stress} = \underbrace{\nu_t}_{Eddy\ Viscosity} \underbrace{\left(\nabla U + (\nabla U)^{T}\right)}_{Mean\ Velocity\ Gradients} - \frac{2}{3}\rho k \underbrace{\delta_{i,j}}_{Kronecker\ Delta} , \tag{2}
$$

2.1. Geometry and Computational Modeling

The wells turbine has a symmetrical geometry with blades equally placed around the circumference. Therefore, the analysis is restricted to a single-blade passage with periodic boundary conditions, as illustrated in Figure 4. The computational domain consists of a straight duct and a 45° segment of the turbine section.
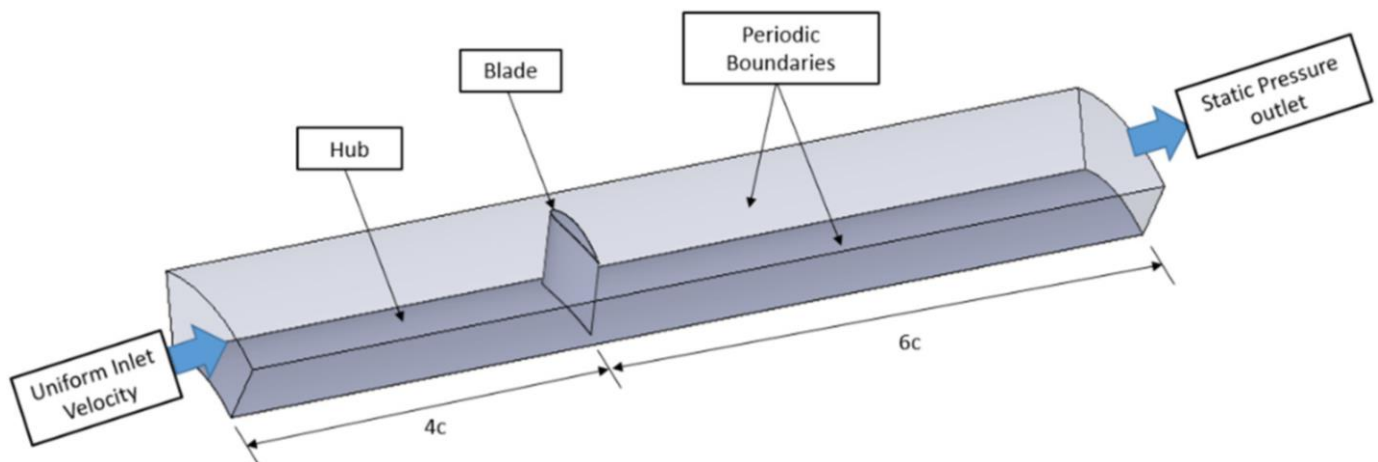

**Figure 4.** Computational domain with boundary conditions [41].

The domain extends upstream and downstream from the blade to 4c and 6c, respectively, in the axial direction. Boundary conditions at the inlet and outlet are specified by uniform velocity profile and static pressure, respectively. Additionally, adiabatic no-slip boundary conditions are applied to the blade surface, hub, and tip. Finally, the computational domain's lateral faces were fitted with a periodic interface. When viewed from the inlet, the turbine rotates counter-clockwise at 2000 r/min. Simulating the rotation of the rotor blades was achieved using the moving reference frame (MRF) method. Since the air was the working fluid, buoyancy forces were not taken into account. A detailed description of the boundary conditions and mesh is provided in Table 2.

Table 2. Meshing with appropriate boundary conditions.

parameters	single turbine
grid	unstructured
prism layers	20
y^+	<1
inlet	uniform velocity
outlet	static pressure
hub, tip, and blade	no-slip wall
convergence criterion	1×10^{-5}

2.2. Mesh Generation

The computational domain must be discretized before solving the governing fluid flow equations. Consequently, there may be discretization errors associated with CFD results. The quality of the computational grids is a significant contributor to numerical analysis errors. ANSYS$^{\text{TM}}$ meshing software is used in this study to generate an unstructured mesh for discretizing the flow domain (Figure 5).

(**a**)   (**b**)
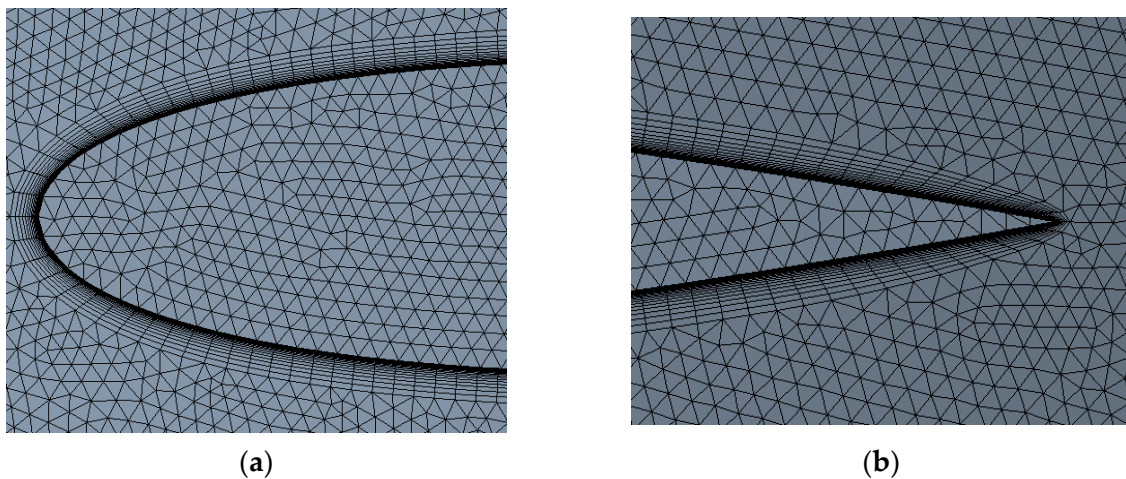
Figure 5. Computational mesh near (**a**) leading edge (LE); (**b**) trailing edge (TE).

A sufficient resolution of the boundary layer flow surrounding the blades is required to predict the dynamic stall point of a turbine accurately. For example, the k-ω SST turbulence model requires a high degree of resolution ($y^+ < 1$) to resolve the viscous sublayer region near the wall accurately. Therefore, prism layers were implemented around the rotor blade surface to capture boundary layer flow.

The dimensionless wall distance, y^+, is defined as follows:

$$y^+ = \frac{yu_T}{\nu},\tag{3}$$

Here, u_T, y, and ν correspond to the friction velocity, the distance of the first layer from the wall (absolute), and the kinematic viscosity of the fluid, respectively. It was determined that the height of the first layer was 1.1×10^{-5} for $y^+ < 1$ using Equation (3). There were 20 layers of prism elements, with a layer growth ratio of 1.2.

A non-dimensional flow coefficient, ϕ, is used to determine the aerodynamic performance, where

$$\phi = \frac{v}{u_{\text{tip}}},\tag{4}$$

changing the inlet axial velocity, v, while maintaining constant circumferential velocity at the tip radius, u_{tip}, resulting in the variation of the flow coefficient, ϕ. A double-precision approach was used for all simulations to minimize rounding errors. Based on the gov-

erning equation's root-mean-square (RMS) residuals, the convergence criterion was set at 1×10^{-5}.

Moreover, the turbine's torque output and pressure drop are monitored to verify that convergence has been achieved. A decrease in the set values assigned to each residual's convergence criterion was necessary in some cases for the monitor quantities to become constant.

The validity of the numerical modeling was assessed for seven separate steady flow configurations based on ϕ. The turbine's operating range was considered as follows: $0.075 \leq \phi \leq 0.275$, or equivalently $4° \leq \alpha \leq 15°$.

Previous literature has demonstrated that some non-dimensional coefficients can be used to assess a turbine's performance. These coefficients are as follows:

The torque coefficient, C_T

$$C_T = \frac{T}{\rho \omega^2 R^5},\tag{5}$$

The Pressure drop coefficient, ΔP_0^*

$$\Delta P_0^* = \frac{\Delta p_0}{\rho \omega^2 R^2},\tag{6}$$

The efficiency, η

$$\eta = \frac{T\omega}{\Delta p_0 Q},\tag{7}$$

where T, Q, Δp_0, c, v, ω, and ρ represent the blade torque, volumetric flow rate, static pressure drop across the turbine, blade chord length, axial inlet velocity, the angular velocity of the turbine, and air density, respectively.

Following is the formula for calculating the Reynolds number:

The Reynolds number, Re

$$Re = \frac{\rho c \sqrt{\left(v^2 + u_{tip}^2\right)}}{\mu},\tag{8}$$

2.3. Grid Independence Study

A grid-independent approach is required to conduct numerical analysis to ensure that the results are accurate. Therefore, we employed four-different grid sizes: coarse (10 mm), medium (5 mm), fine (2.5 mm), and extra-fine (1.25 mm).

Then, a comparison was performed here between the calculated torque coefficient and available experimental and numerical data at $\phi = 0.225$. A coarse grid (3.6 million cells) demonstrated a significantly lower torque coefficient than a medium grid (7.6 million cells). In addition, the number of cells for the fine mesh nearly doubled with a 50% reduction in cell size, resulting in less variation in torque coefficient. Furthermore, there were no significant differences between extra-fine and fine grids. Finally, the discrepancies observed were ~24%, ~4%, and ~0.5% between the medium, fine, and extra-fine grids. Therefore, the extra-fine grid was used for the subsequent simulations. A test of the grid dependency can be found in Figure 6.
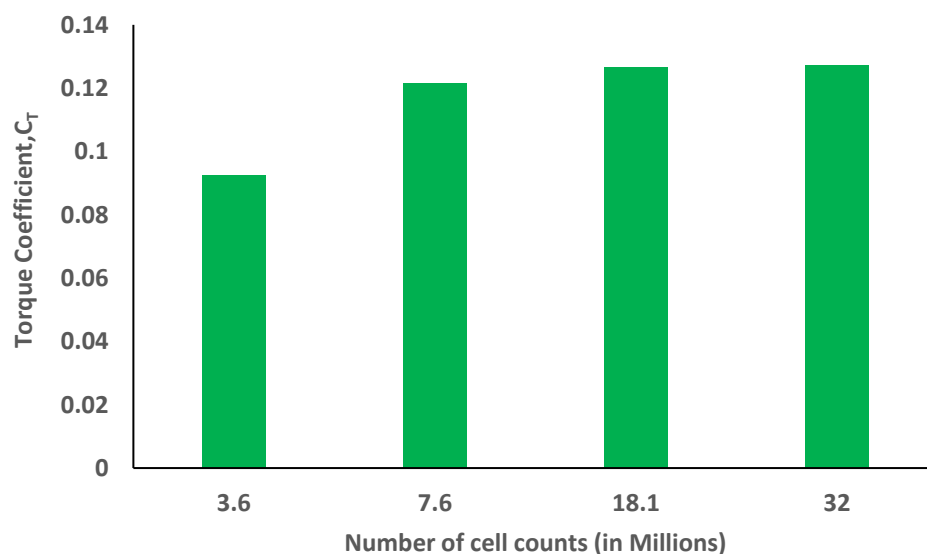
**Figure 6.** Grid independence study at $\phi = 0.225$.

The numerical uncertainty was evaluated using grid convergence index (GCI) based on Richardson's extrapolation method [42]. Reference [43] provides details regarding the GCI. Table 3 presents the uncertainty assessment based on the GCI. In addition, the GCI and averaged relative errors for the fine grid (5.2% and 7.9%, respectively) are significantly lower than those for the medium grid (40.9% and 42.7%, respectively). Nonetheless, grid convergence requires a GCI value of less than 3% between the grids [44]. For the extra fine grid, the calculated GCI and extrapolated relative errors were 0.58% and 0.96%, respectively, so it was chosen for subsequent simulations.

Table 3. Uncertainty estimation.

Grid size (mm)	Extra fine, Fine, Medium, and Coarse	1.25, 2.5, 5.0, 10.0
Average cell size (h)	h_1, h_2, h_3, h_4	8×10^{-4} m, 0.0017 m, 0.0033 m, 0.0057 m
Grid refinement factor (r)	r_{21}, r_{32}, r_{43}	2.07, 1.9681, 1.7318
Performance parameter (ϕ)	ϕ_1, ϕ_2, ϕ_3, ϕ_4	0.1273, 0.1267, 0.1216, 0.0925
Apparent order	p	2.83
Approximate relative error	e_a^{21}, e_a^{32}, e_a^{43}	0.0050, 0.0403, 0.2393
Extrapolated values	ϕ_{ext}^{21}, ϕ_{ext}^{32}, ϕ_{ext}^{43}	0.1279, 0.1319, 0.1613
Extrapolated relative error	e_{ext}^{21}, e_{ext}^{32}, e_{ext}^{43}	0.0096, 0.0787, 0.4268
GCI	$GCI_{extrafine}^{21}$, GCI_{fine}^{32}, GCI_{medium}^{43}	0.0058, 0.0520, 0.4088

### 2.4. Validation of Numerical Modeling

At constant rotational speeds of 2000 rpm, this study evaluated turbine performance at various axial inlet velocities. The flow coefficient varied from $0.075 \leq \phi \leq 0.275$, which corresponds to the change in Reynolds number from 5.25×10^5 to 5.43×10^5. A comparison of the present CFD results with experimental and numerical data is undertaken to validate the results by evaluating the pressure-drop coefficient (ΔP_0^*), torque coefficient (C_T), and efficiency (η) values, as shown in Figure 7.
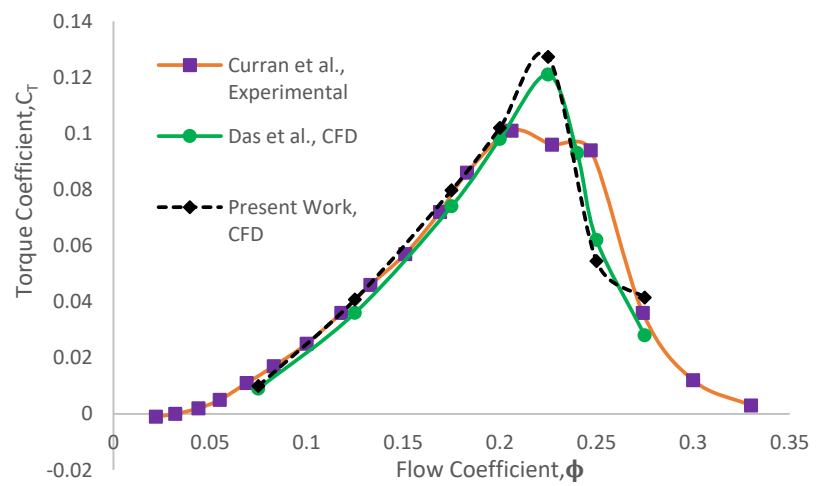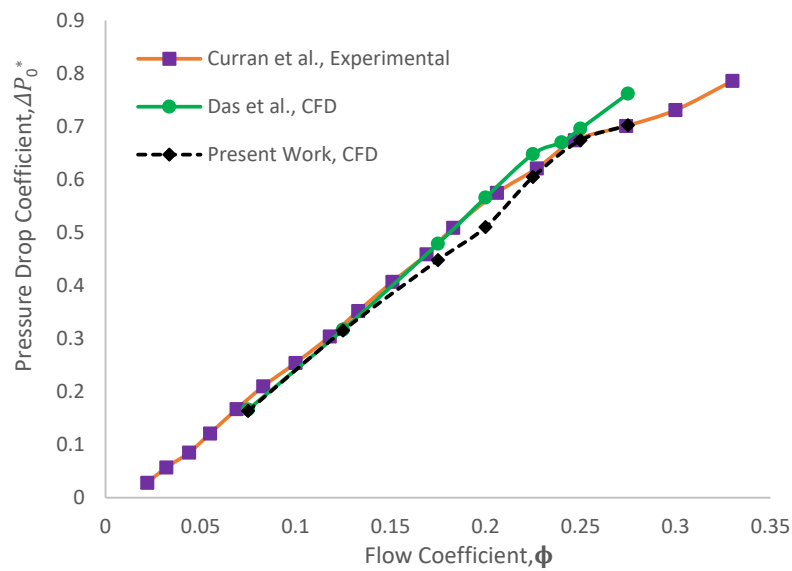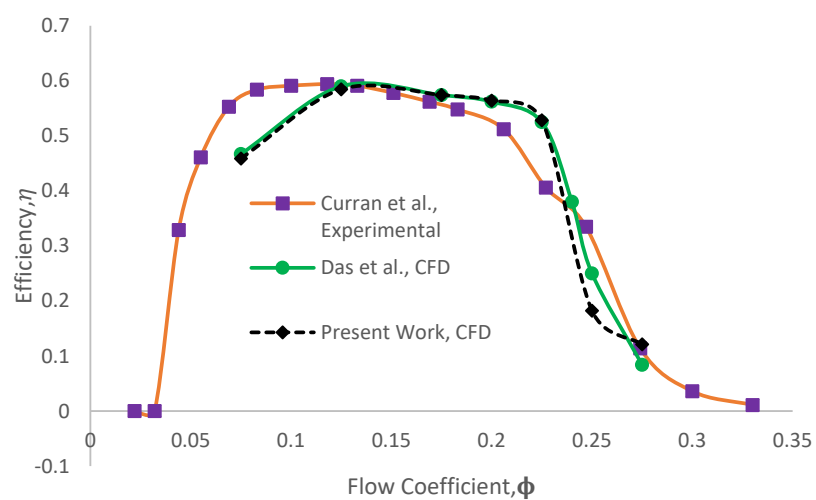
Figure 7. Validation of present CFD data with experimental and numerical results at $\phi = 0.225$ for various non-dimensional parameters (**a**) C_T; (**b**) ΔP_0^*; and (**c**) η.

Up to the flow coefficient, $\phi < 0.225$, the current numerical findings agree well with the experimental data. Figure 8 displays the error percentage with the existing experimental [5] and numerical data [39]. Additionally, the mean absolute percentage error (MAPE) is utilized to determine the discrepancy between experimental and numerical results. The non-dimensional torque, pressure drop, and efficiency obtained from our numerical simulations exhibit a maximum discrepancy of approximately 8% from the experimental outcomes and numerical data until the flow stalls.
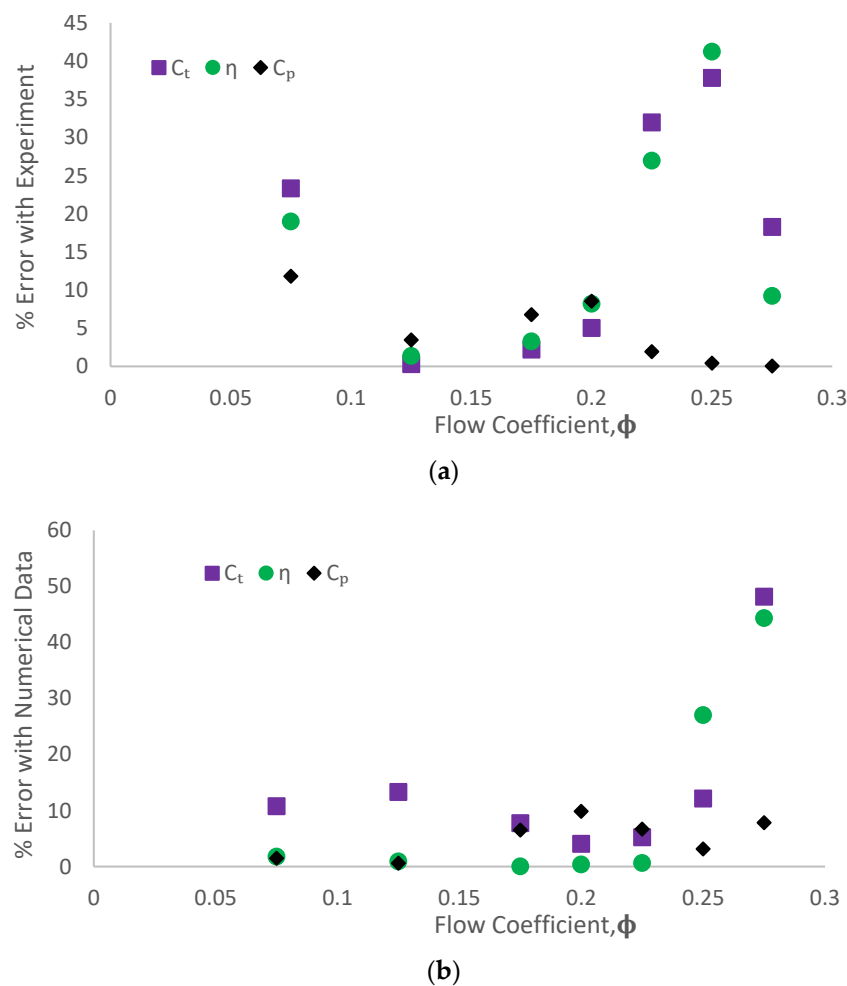

(a)

(b)

Figure 8. Percentage of error with (**a**) experimental [5]; (**b**) numerical data [39].

In the case of $\phi \geq 0.225$, the angle of attack (AOA) is relatively large. Consequently, deep stalling occurs due to the flow separation at the leading edge, rapidly dropping torque and efficiency. Due to the nature of RANS solvers, they are not very good at predicting adverse pressure gradient flow separations and often overestimate torques. As a result, numerical results become increasingly difficult to reconcile with experimental results at stalled flow conditions [5]. Despite this, the results of the present study are comparable to those obtained by other CFD [20,22,39] studies, given the same geometrical features.

Furthermore, to validate the fidelity of our results, the baseline turbine with a rectangular GF (flap height = 1.5%c, flap width = 0.5%c) was simulated and compared to the findings of previous studies in the literature [20,22]. The results of our simulations were in good agreement with these studies, as demonstrated in Figure 9. This comparison confirms the reliability of our results and underscores the accuracy of our simulation methodology.
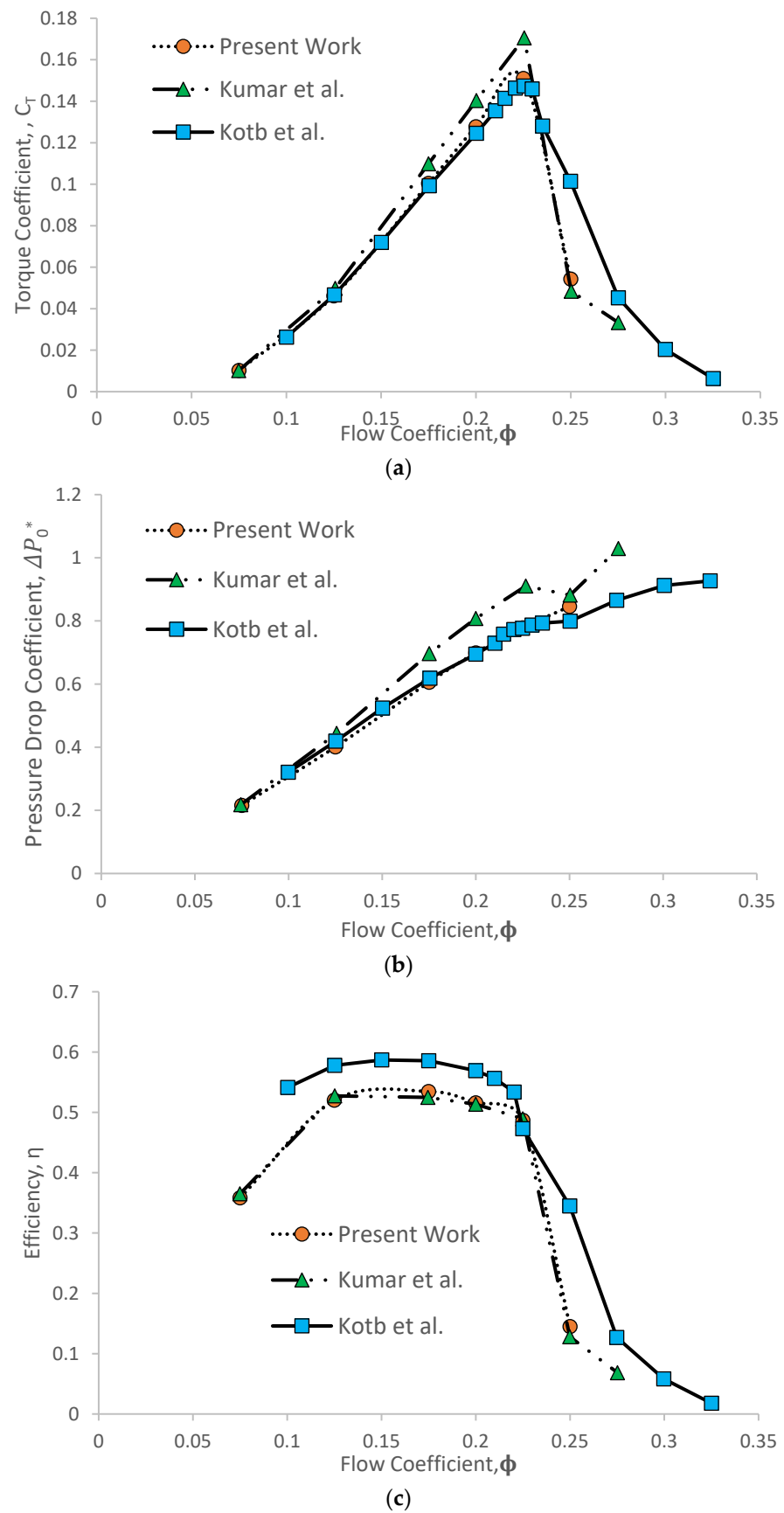
Figure 9. Verification of our simulation results for the baseline turbine with a rectangular GF through (**a**) C_T; (**b**) ΔP_0^*; (**c**) η.

3. Results

Once the numerical results had been validated, we simulated our new turbine designs for a range of flow coefficients, $0.075 \leq \phi \leq 0.3$, or equivalently $4.3° \leq \alpha \leq 16.7°$. We examine the two designs, one using GF attached to a baseline and the other using GF attached to a hybrid, and compare them with the other using constant chord (baseline), as illustrated in Figure 10.
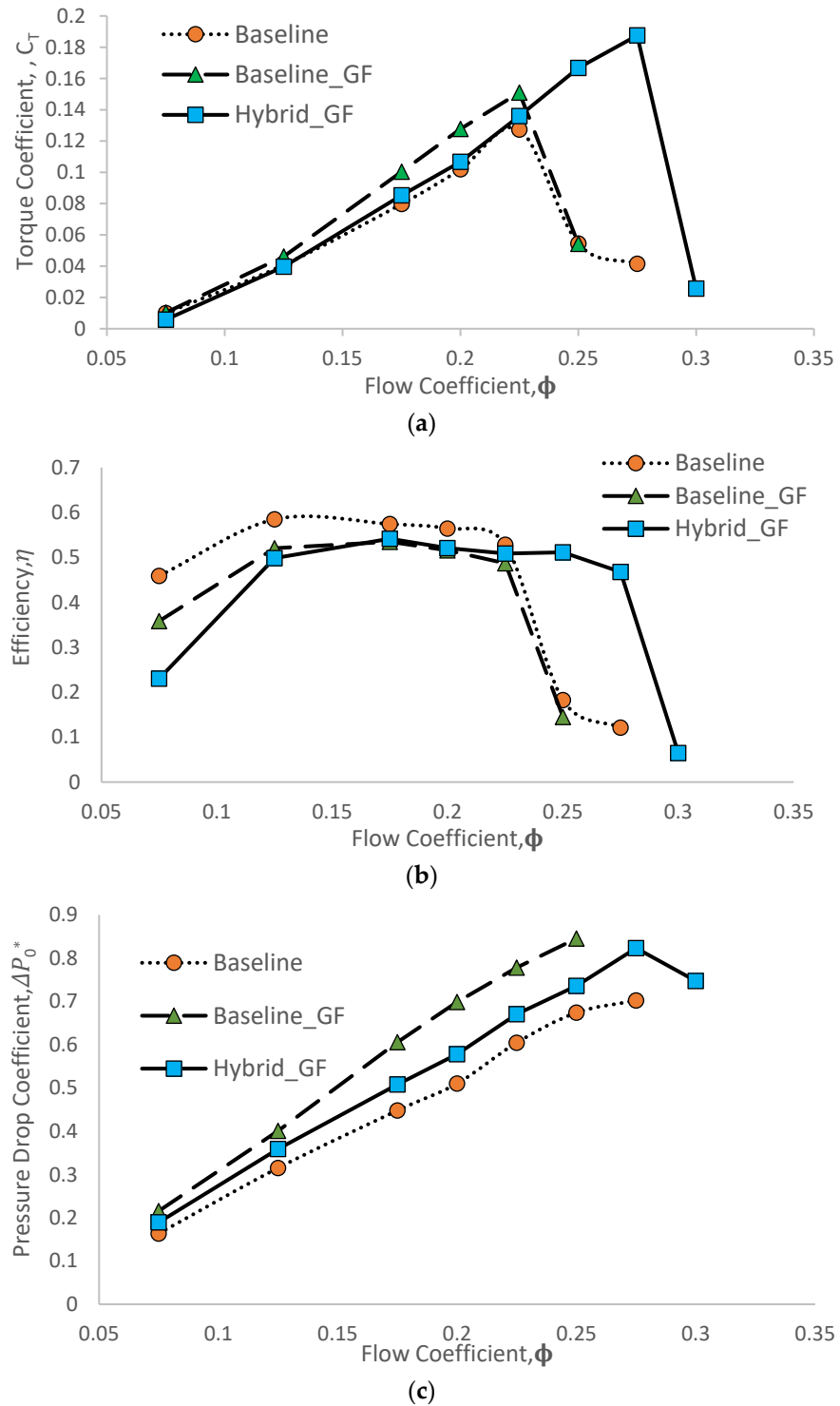
(a)

(b)

(c)

Figure 10. Comparison of results of turbines for various non-dimensional parameters (**a**) C_T; (**b**) η; (**c**) ΔP_0^*.

3.1. Quantitative Analysis

Figure 10a shows that the GF caused an enhanced maximum torque coefficient $C_{T,max}$ of ~19% and ~47% for the baseline and hybrid, respectively, compared to the baseline (without GF). However, the increased pressure drop incurred a penalty in peak efficiency than the baseline. The GF impacted and reduced the baseline and the hybrid turbine's peak efficiency by ~9% and ~7%, respectively.

Moreover, the GF extended the operating range by ~3° AOA for the hybrid turbine. That means the hybrid turbine with GF stalled at $\phi = 0.3$, whereas the other designs experienced the stall at $\phi = 0.250$.

The baseline operates at the highest efficiency within its operating range. However, unlike others, the hybrid turbine with GF maintains a constant efficiency before it stalls, as shown in Figure 10b.

According to Figure 10c, a linear relationship exists between the pressure-drop coefficient ΔP_0^* and flow coefficient ϕ. The baseline with GF produces the highest pressure drop, followed by the hybrid turbine with GF and baseline.

3.2. Flowfield Analysis

Figure 11 depicts the streamlines on the suction surface of three different designs of turbine blades concerning pre–stall and stall conditions that correspond to their respective flow coefficients. For example, at a flow coefficient of $\phi = 0.225$, the flow separation phenomenon is initiated at the hub region close to the leading edge of the baseline turbine suction side. In contrast, the baseline turbine that employs GF displays vortex shedding as two counter-rotating vortices are visible in the vicinity of the hub, which implies an imminent occurrence of blade stall. However, a significant amount of flow separation is evident for the hybrid turbine with GF, as a strong vortex has appeared near the blade tip. As per the stalling behavior, the blade tip rather than the hub experiences the stall initiation first. Accordingly, the hybrid turbine has presented the onset of unavoidable flow separation when subjected to adverse pressure gradients at $\phi = 0.275$.

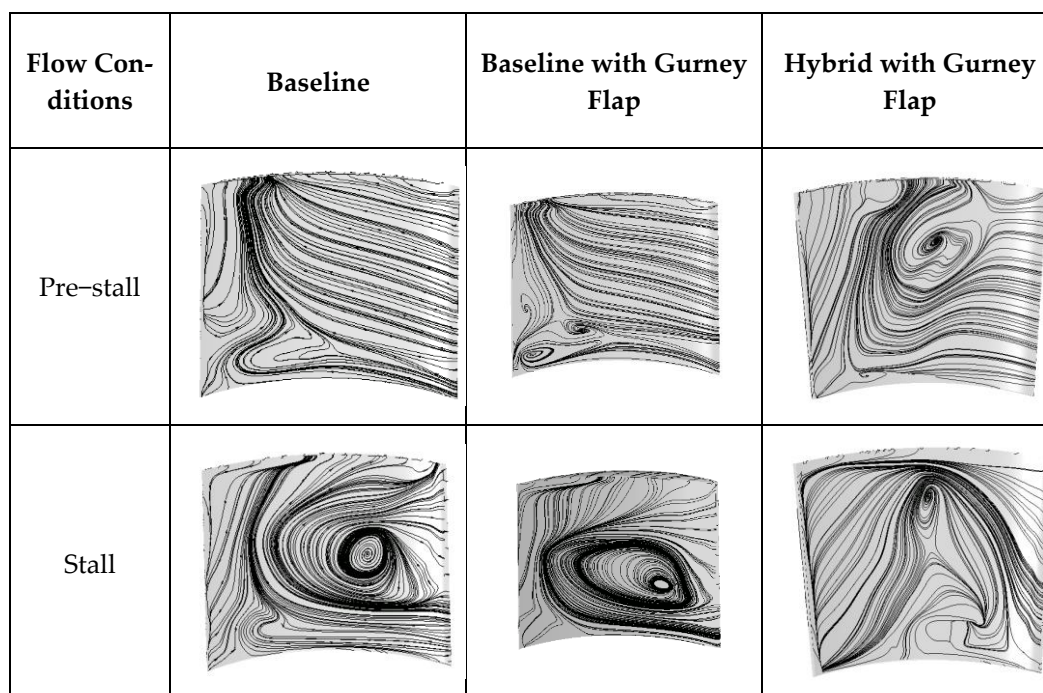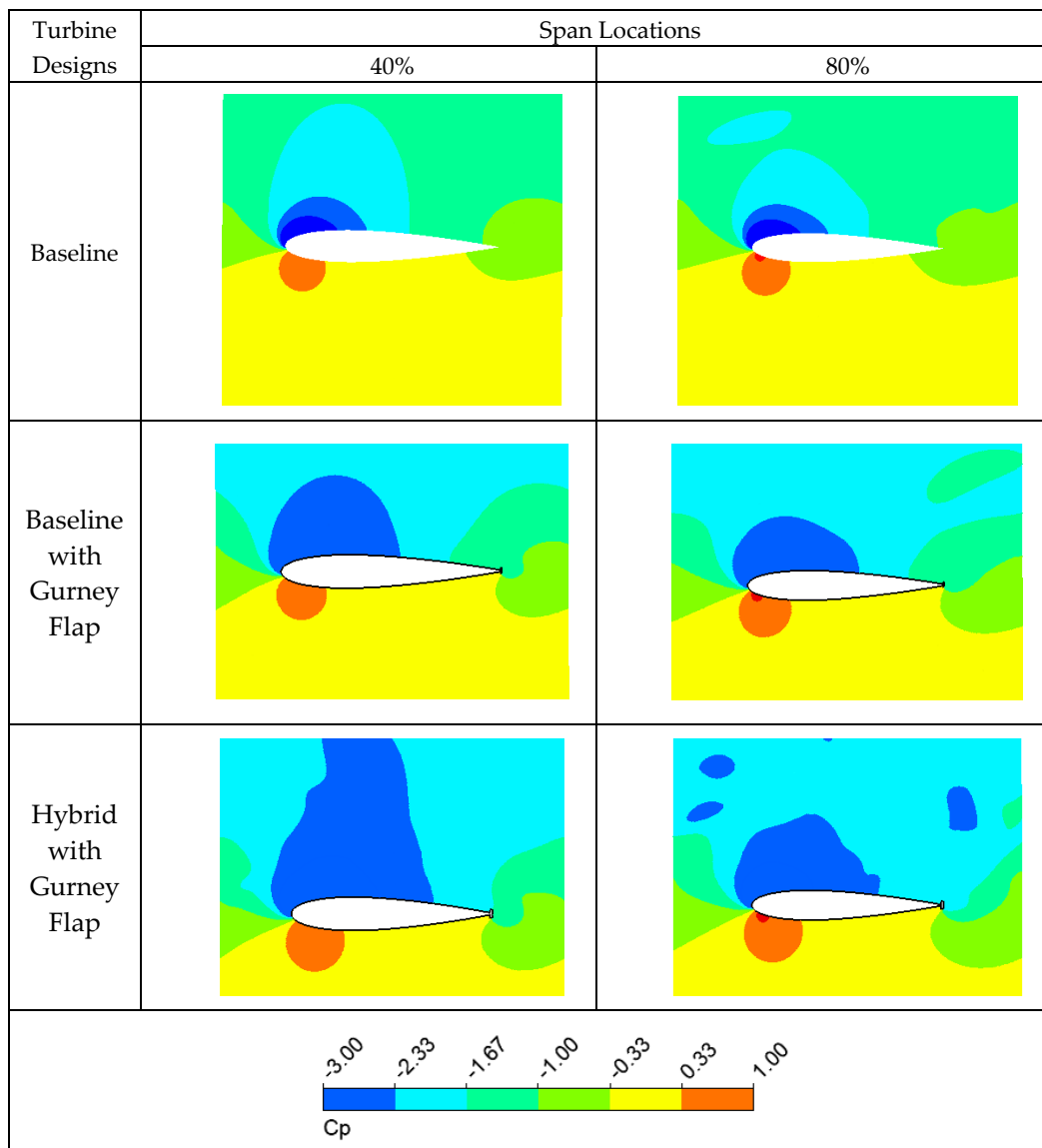| Flow Conditions	Baseline	Baseline with Gurney Flap	Hybrid with Gurney Flap
Pre–stall			
Stall			

Figure 11. Streamlines in blade suction surface at pre–stall and stall flow conditions.

As the flow coefficient was elevated to $\phi = 0.250$, corresponding to a large AOA (14°), a powerful vortex appears near the leading edge of the baseline turbine blade, with the vortex

center located at roughly the mid-span. This led to the stall occurrence in the baseline turbine, considerably reducing torque and efficiency. In addition, the baseline turbine incorporating GF also undergoes stall, accompanied by a significant flow recirculation pattern, with the vortex center at approximately 40% span. Furthermore, the flow separates, recirculates, and vortices move further up to the tip for the hybrid turbine utilizing GF; the turbine loses torque and efficiency substantially at ϕ = 0.3.

Performing detailed analyses of the turbine flow field under different conditions, such as varying flow coefficients, assists in establishing a fundamental understanding of the aerodynamic performance of the baseline and turbines employing GF. For instance, Figure 12 demonstrates the contours of the static pressure coefficient at different span locations (i.e., 40% and 80% of the span distance from the hub) under three distinct flow coefficients.

(a)

Figure 12. *Cont.*
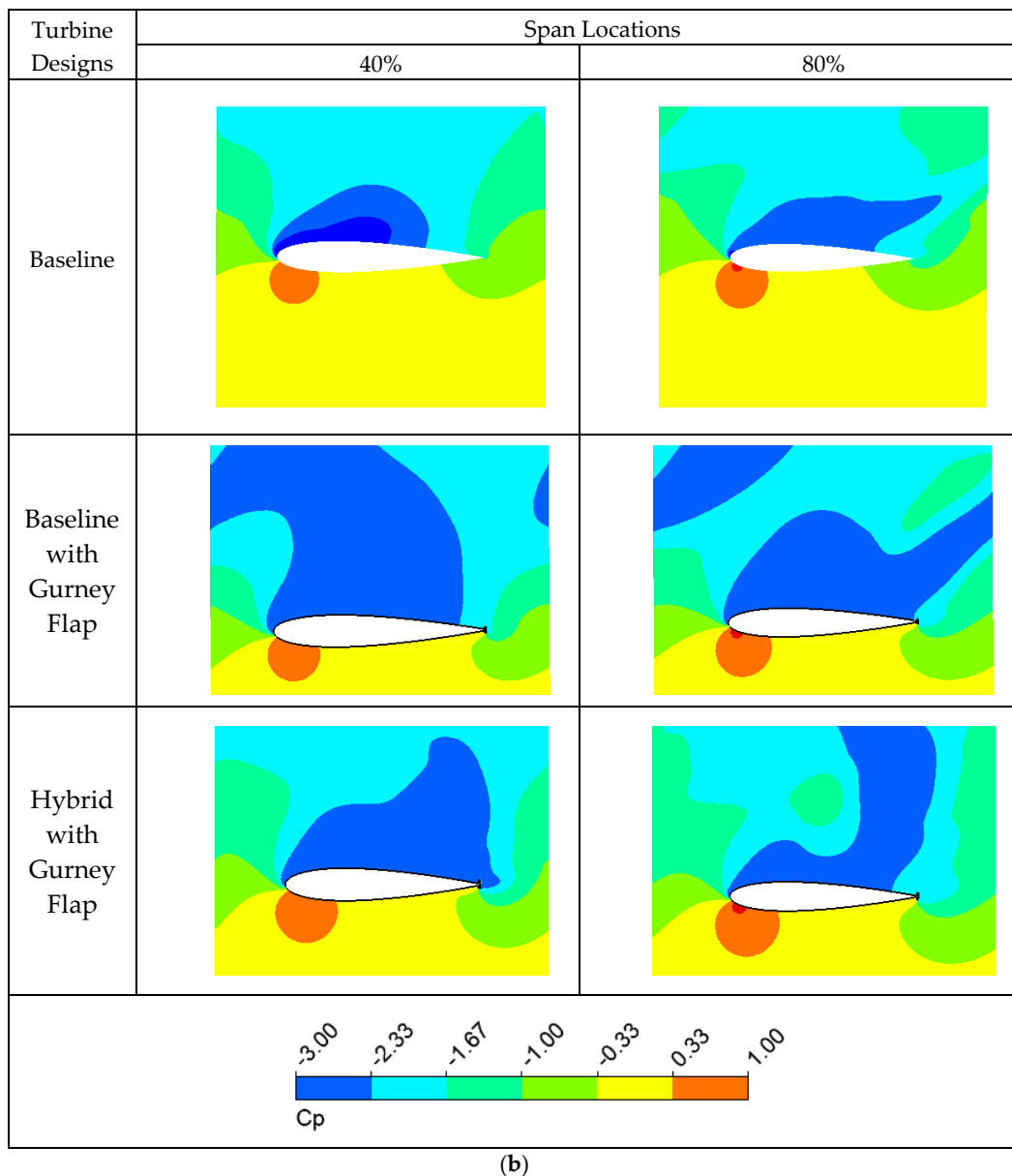
Turbine Designs	Span Locations	
	40%	80%
Baseline		
Baseline with Gurney Flap		
Hybrid with Gurney Flap		

(**b**)

Figure 12. Contours of C_P at various span locations for (**a**) pre–stall; (**b**) stall flow conditions.

The static pressure coefficient, C_P, is defined as follows:

$$C_P = \frac{P - P_\infty}{\frac{1}{2}\rho_\infty v_\infty^2},\tag{9}$$

When the flow impinges on the blade's leading edge, it results in a stagnation point. At this point, the static pressure is at its maximum, while the velocity is zero. As a result, a region of high pressure, also known as the pressure side (PS), is present on the lower surface of the airfoil. This high-pressure region expands as the flow coefficient increases, corresponding to a rise in inlet axial velocities. Conversely, a low-pressure zone develops on the suction surface (SS), which is the top surface of the airfoil. The air moves from the PS to the SS while trying to maintain its attachment to the blade surface.

At the flow condition just prior to stall, the baseline turbine exhibits the smallest low-pressure region relative to the other turbines on the SS of the blade, as seen in Figure 12a. This indicates that the baseline is less prone to flow separation and stall initiation than the

other turbines. In addition, this observation suggests that the baseline may have a more favorable pressure distribution than the other turbines under similar operating conditions.

At the 40% span locations of the blade, no significant discrepancy is detected on the PS between the baseline turbine and the baseline turbine with GF. This indicates that the addition of GF to the baseline turbine does not lead to any noticeable changes in the pressure distribution on the PS of the blade at the aforementioned spanwise location. However, the GF attached to the hybrid turbine caused a significantly greater low-pressure and high-pressure zone in the SS and PS, respectively.

At the 80% span location, the imminence of the stall is more evident with added low-pressure zones and vortices appearing on the SS. However, the flowfield on the PS remains unchanged for all the turbine blades.

Figure 12b illustrates that at $\phi = 0.250$, the baseline turbine has an extended low-pressure zone (approximately 90% and 100% from the blade LE to TE) for the 40% and 80% span locations, respectively. Furthermore, the high-pressure zone begins to bleed onto the SS, causing an adverse pressure gradient that leads to the flow separation and blade stall, resulting in decreased aerodynamic performance. In the baseline incorporating a GF, it can be observed that at a span location of 40%, the low-pressure region covers roughly 90% of the chord, and at an 80% span location, it covers the entire chord. As a result, some of the airflows bleed toward the SS. This leads to the formation of a strong vortex in the wake of the GF at the trailing edge (TE). On the contrary, for the hybrid turbine with GF, the entire chord gets covered with low-pressure zones in its SS at $\phi = 0.3$. Moreover, as the assigned span location moves closer toward the tip, the level of flow separation also increases.

Figure 13 depicts the flow field of a blade for each turbine using C_p contours and streamlines at different planes passing through 25%, 50%, and 75% of the blade's chord. The C_p contours represent the pressure coefficient distribution on the blade's surface, with regions of low pressure indicated by negative values and regions of high pressure indicated by positive values. The expansion of low-pressure zones is directly proportional to increasing flow coefficients. The streamlines represent the path taken by fluid particles as they move through the flow field, thereby allowing us to gain insights into the complex fluid dynamics that are taking place. By following the streamlines, we can see how the fluid flows toward the blade, interacts with its surface, and changes direction and velocity as it moves away from the blade. This information is essential for understanding the aerodynamics of blades and can be used to optimize their design for improved performance.

The baseline turbine exhibits the highest suction pressure and the smallest low-pressure region across the blade's span at all designated chord locations. This indicates that the baseline turbine has a more favorable pressure distribution, with a greater suction force that pulls in more fluid toward the blade. The smaller low-pressure region also suggests that there is less flow separation and better attachment of the flow to the blade surface, which can lead to the more efficient operation of the turbine.

Under pre–stall conditions, the streamlines on the SS of the turbine blades are remarkably similar for all turbines at the 25% chord location. This indicates that the flow field in this region is largely unaffected by differences in the design of the turbines. However, a small clockwise vortex is observed to form near the tip of the baseline turbine blade, in contrast to the other turbines.

As the chord location increases from 25% to 50%, this vortex becomes stronger, and a counter-clockwise vortex is visible near the hub. The formation of the counter-rotating vortices is a precursor to flow separation. Despite the appearance of the vortices, the flow remains attached to the blade surface. Finally, at 75% chord, the flow begins to separate near the blade's tip, indicating a significant deviation from the flow behavior observed at earlier chord locations.
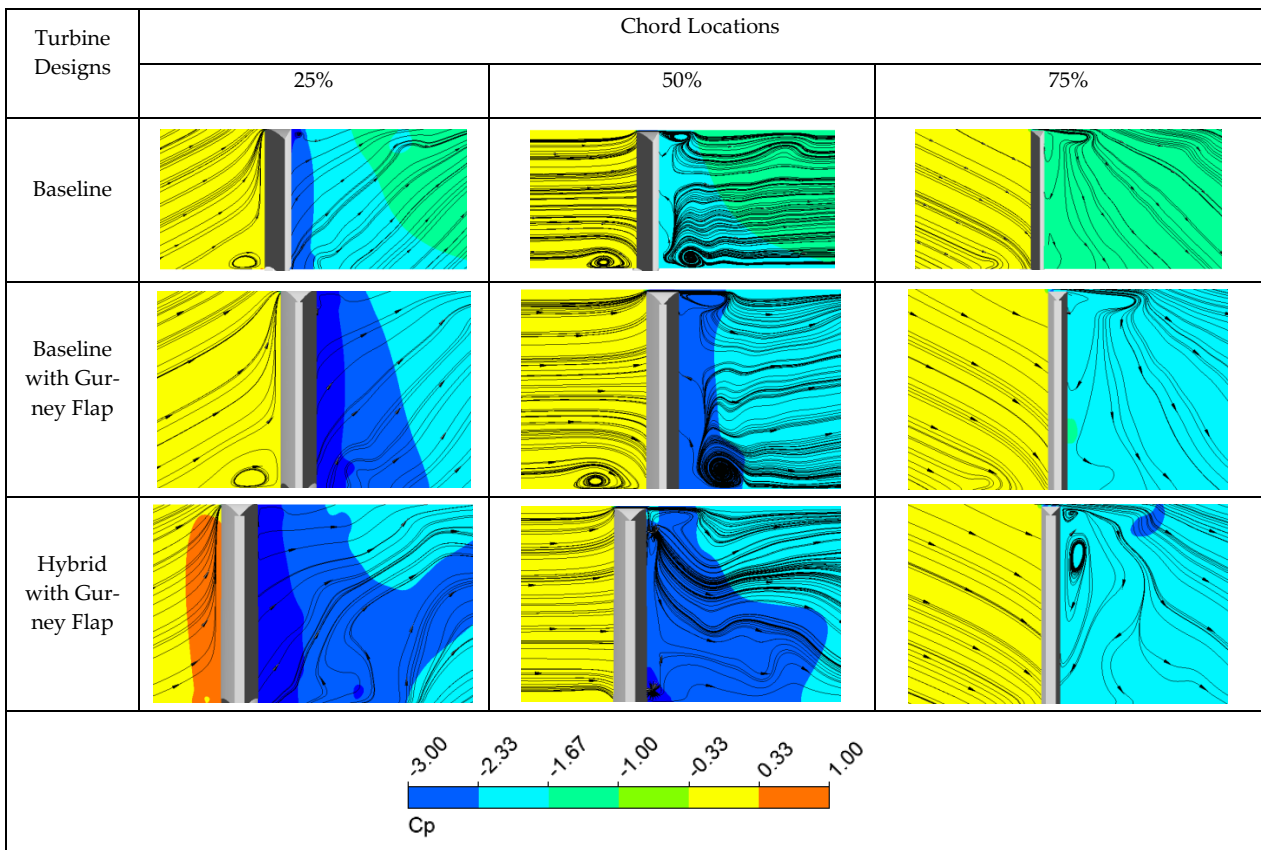
(**a**)
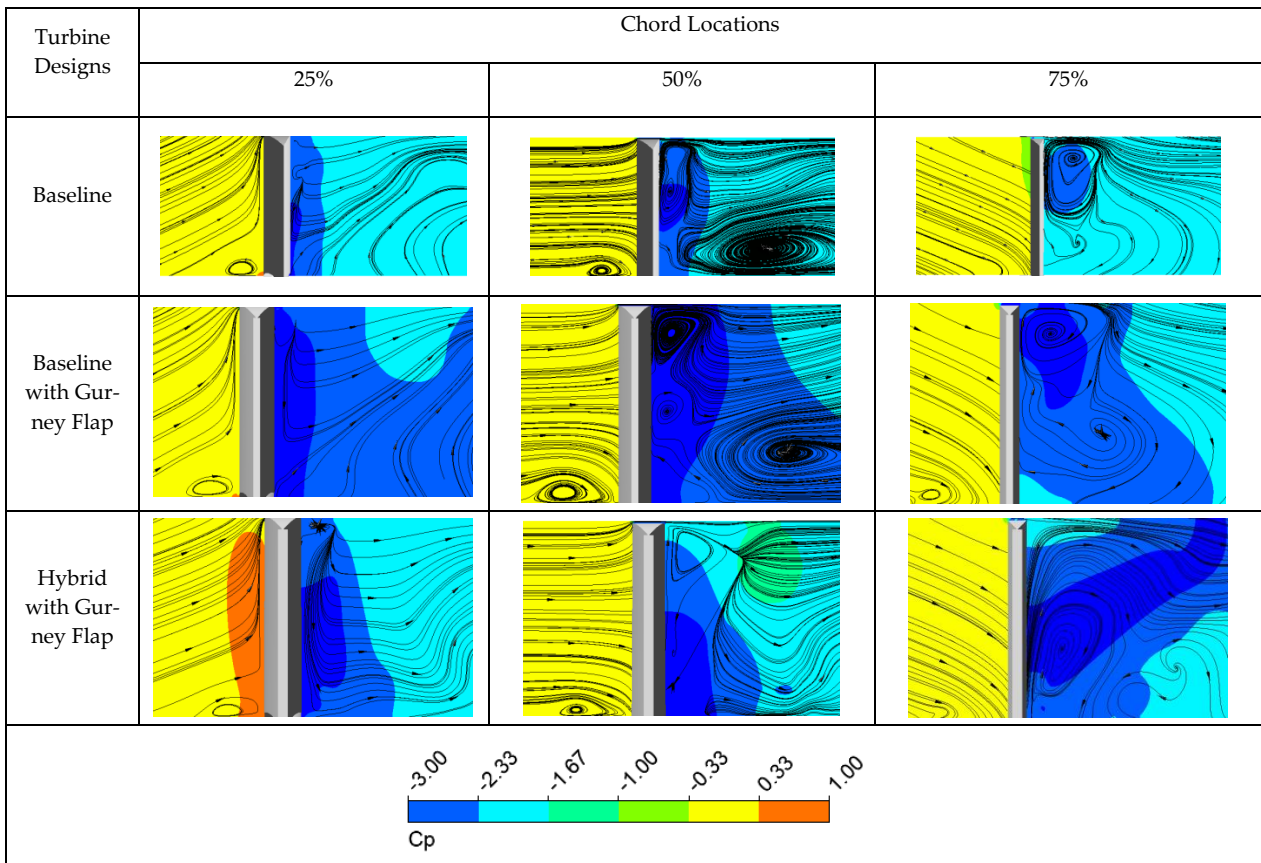
(**b**)

Figure 13. Contours of C_P and streamlines at various chord locations for (**a**) pre–stall; (**b**) stall flow conditions.

Similarly, at 50% chord, under pre–stall conditions, counter-rotating vortices are observed near the blade tip and hub in the baseline turbine configuration equipped with GF but with increased intensity compared to the baseline configuration. These vortices are responsible for flow separation near the blade surface. However, in the case of the hybrid turbine with GF, the counter-rotating vortices appear at 75% chord; the flow reattaches along the span.
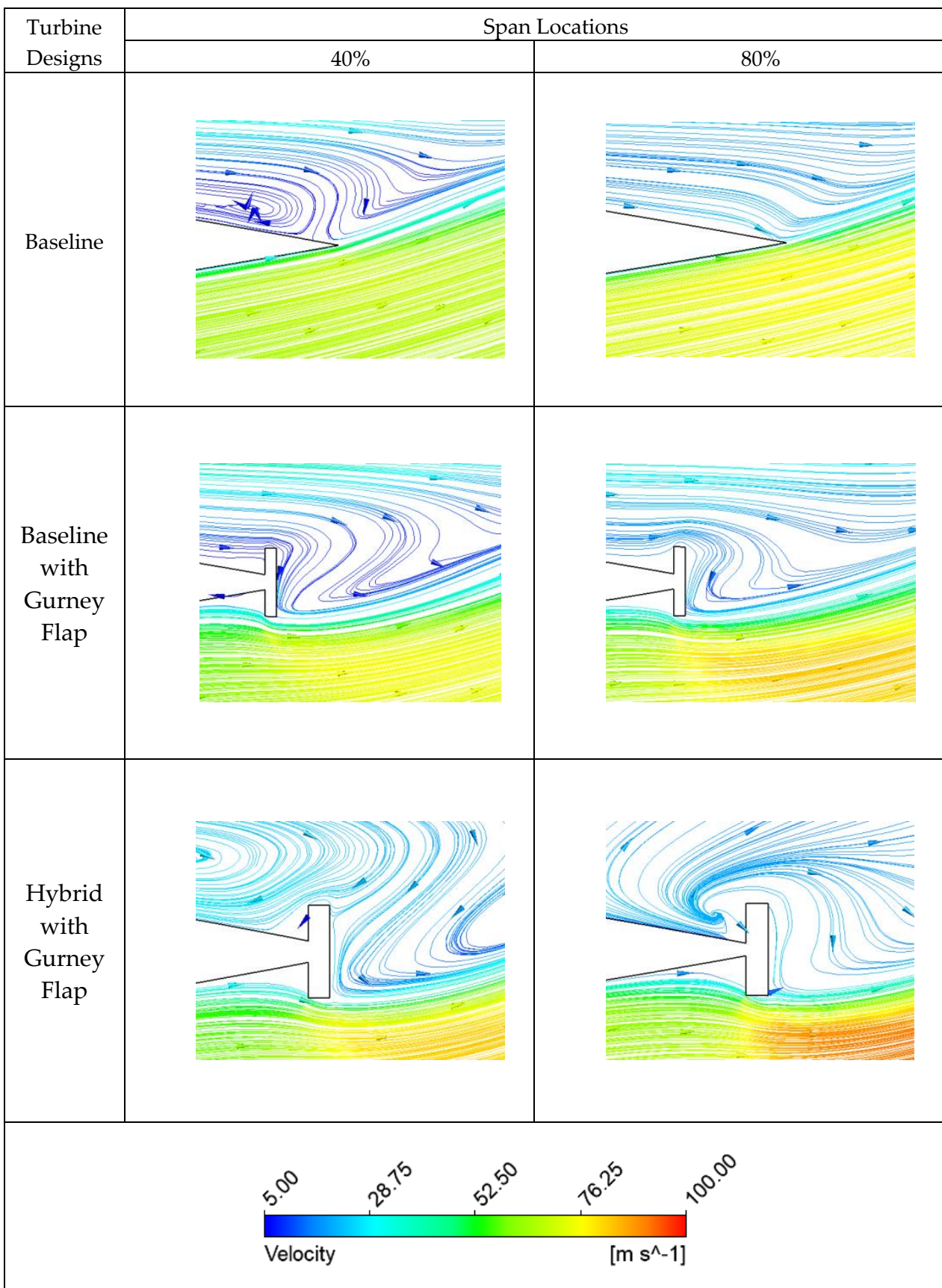
At ϕ = 0.250, the low-pressure zones near the blade surface continue to expand, resulting in an adverse pressure gradient. This adverse pressure gradient causes the flow to separate from the blade surface and leads to blade stalls for both the baseline and baseline, incorporating GF configurations. The flow separation is accompanied by the formation of multiple vortices that span the entire blade span at the 50% and 75% chord locations.

However, at ϕ = 0.3, the whole span is covered by low-pressure zones on the SS of the hybrid turbine blades equipped with GF. At the 50% chord location, a strong clockwise vortex is observed near the blade's tip. This vortex expands throughout the blade span and is accompanied by the formation of a counter-clockwise vortex near the hub. The counter-rotating vortices induce vortex shedding, which can result in increased noise production, flow separation, and blade stall. In addition, at 75% chord, a clockwise vortex is observed that covers almost 80% of the blade span.

Figure 14 presents a visualization of the flow phenomenon occurring along the blade chord of each turbine. The flow field is investigated at various flow coefficients through the utilization of velocity-colored streamlines at two distinct planes situated at 40% and 80% of the blade's span. This enables us to examine how air moves across the blade span, providing insight into the blade's aerodynamic behavior under different flow conditions. Under pre–stall flow conditions, a clockwise vortex has appeared in the vicinity of the TE on the SS at 40% span for the baseline, but the flow remains attached to the blade surface at 80% span. However, there are no appreciable changes in the streamline patterns observed at the 40% and 80% span locations for the baseline with GF. Notably, the GF has pushed the vortex downstream by energizing the boundary layer, which essentially enhances the torque generation. On the contrary, for the hybrid turbine, a clockwise and an anti-clockwise vortex are observed upstream and downstream of the GF, respectively.
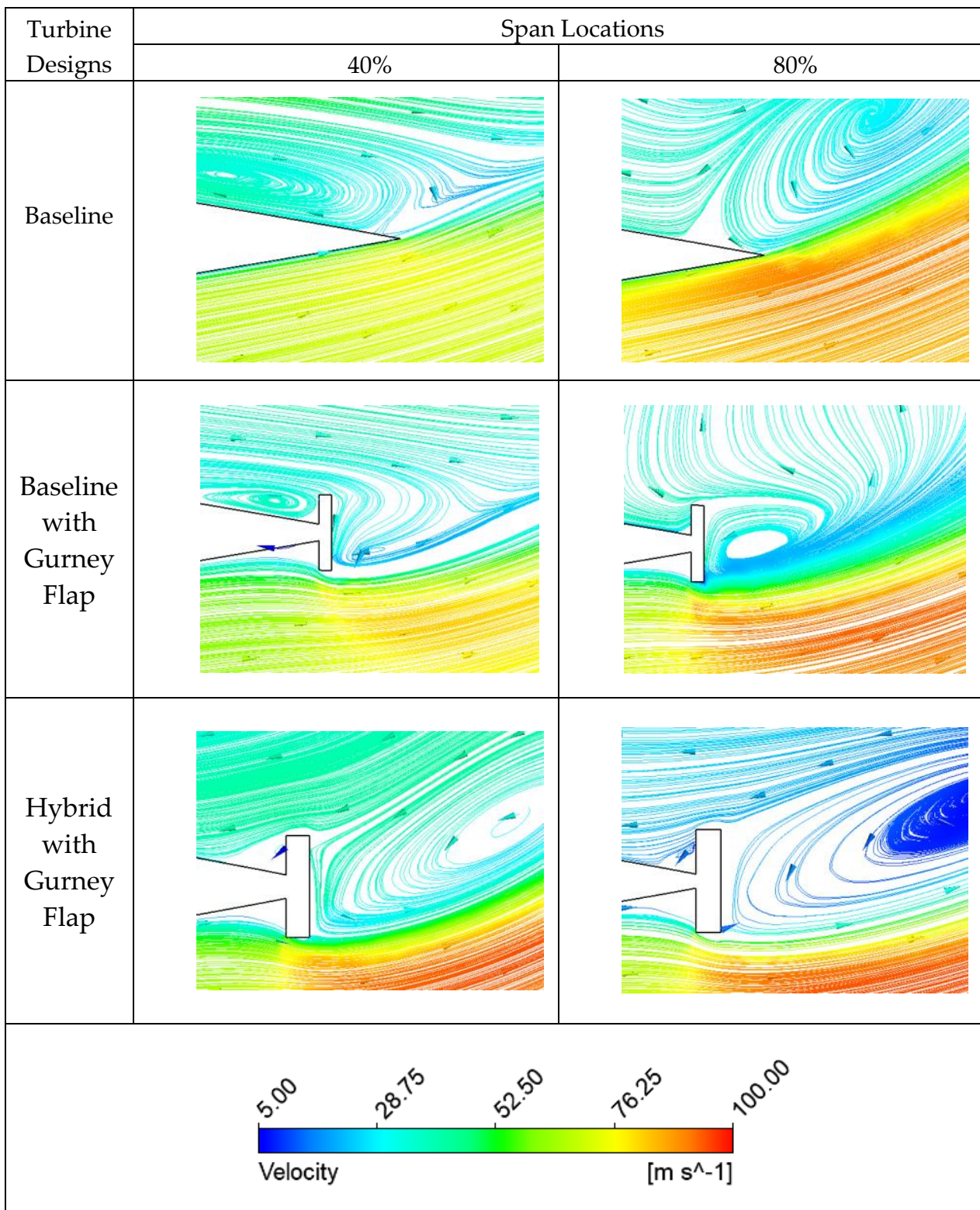
At stall flow conditions, flow separation on the blade surface of turbines is a common occurrence, with the separated flow forming a vortex at the blade's TE, as observed in all turbine blades. As the stall condition progresses, the separation region expands towards the blade tip, and the strength of the vortex increases, shifting towards the blade's LE. The development of the vortex is due to a combination of factors, including the interaction of the separated flow with the blade geometry, as well as the formation and shedding of vortices in the wake of the blade. The resulting vortex significantly impacts the turbine's performance, leading to a drastic drop in torque as the blade stalls.

Wall shear stress plots are an essential tool for studying flow separation, a phenomenon that occurs when the flow separates from the surface of a solid body, leading to the formation of eddies and vortices. Wall shear stress is a measure of the frictional force acting between the fluid and the surface of the solid body, and it provides important insights into the behavior of the flow near the wall. Based on the analysis of wall shear stress plots, as shown in Figure 15, it has been observed that flow separation typically initiates at a critical flow coefficient of ϕ = 0.225 for the baseline and baseline with GF. At the 10% span, the flow separation points are at x/c = 0.61, and the flow reattaches close to the blade's TE. On the other hand, for the hybrid turbine with GF, wall shear equals zero, representing flow separation at x/c = 0.86 for ϕ = 0.275.

Turbine Designs	Span Locations	
	40%	80%
Baseline		
Baseline with Gurney Flap		
Hybrid with Gurney Flap		

(**a**)

Figure 14. *Cont.*

Turbine Designs	Span Locations	
	40%	80%
Baseline		
Baseline with Gurney Flap		
Hybrid with Gurney Flap		

(**b**)

Figure 14. Streamlines at different span locations for (**a**) pre–stall; (**b**) stall flow conditions.

Span Location	Pre–Stall Flow Conditions
10%	
40%	
80%	

(**a**)

Figure 15. *Cont.*

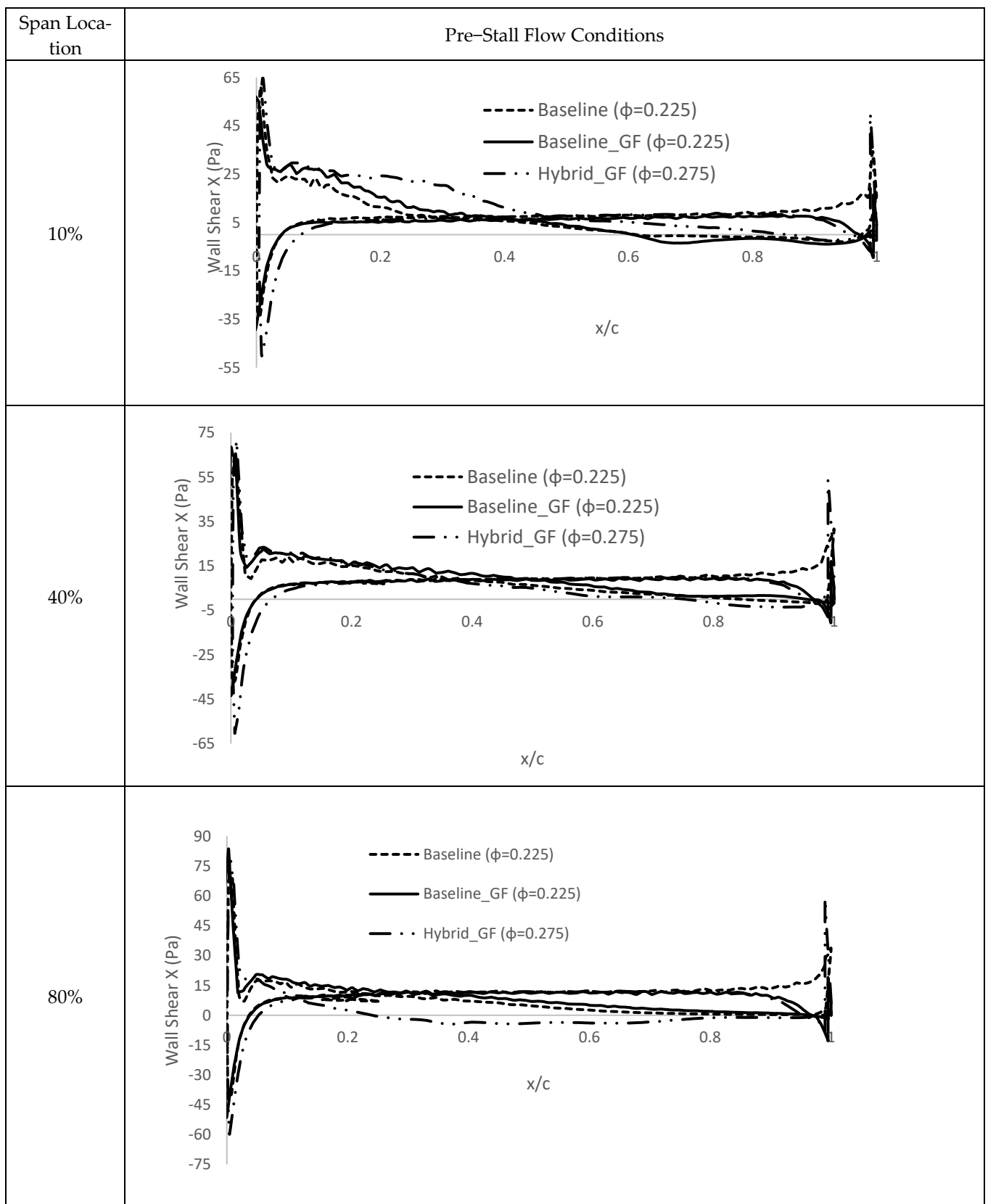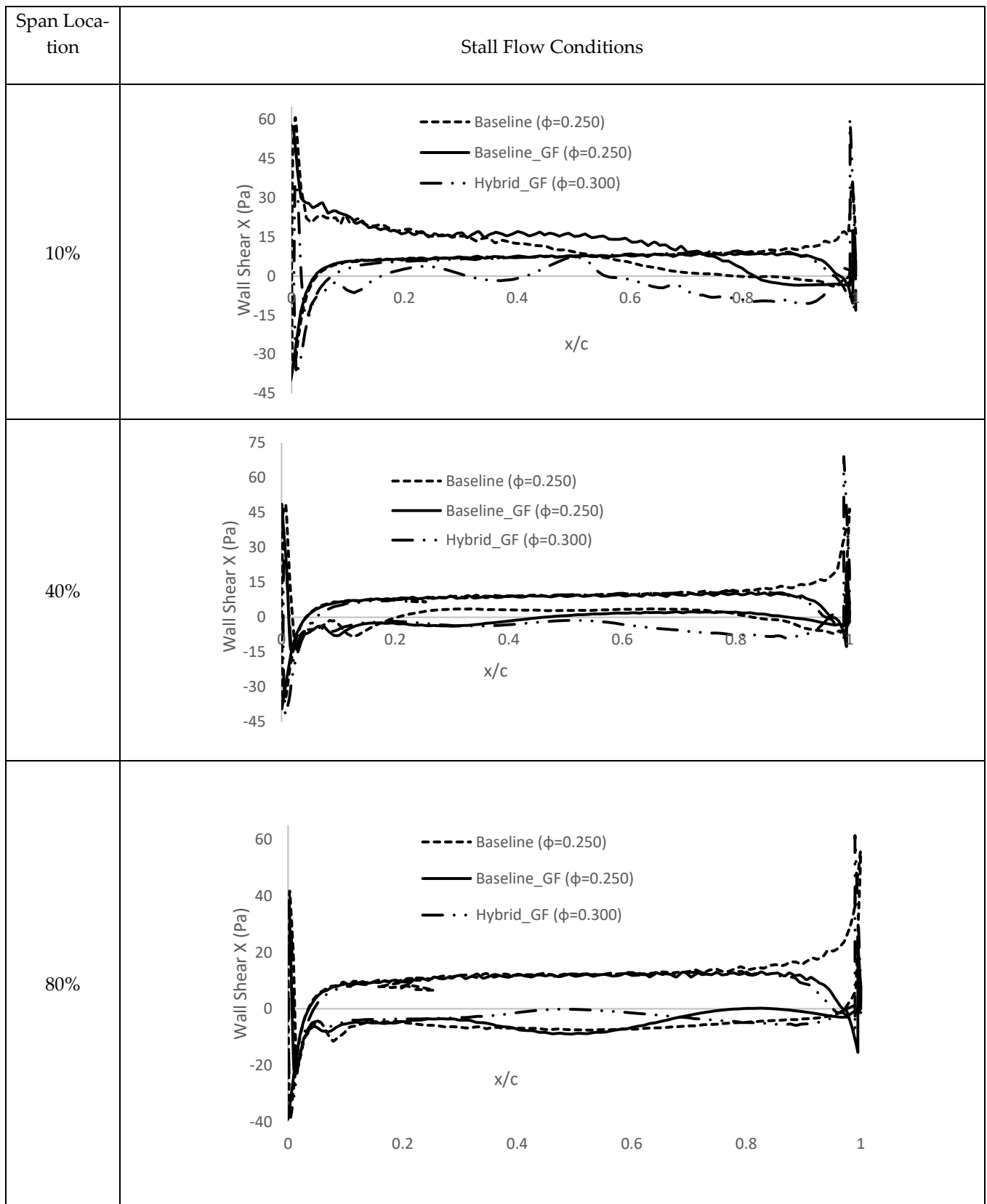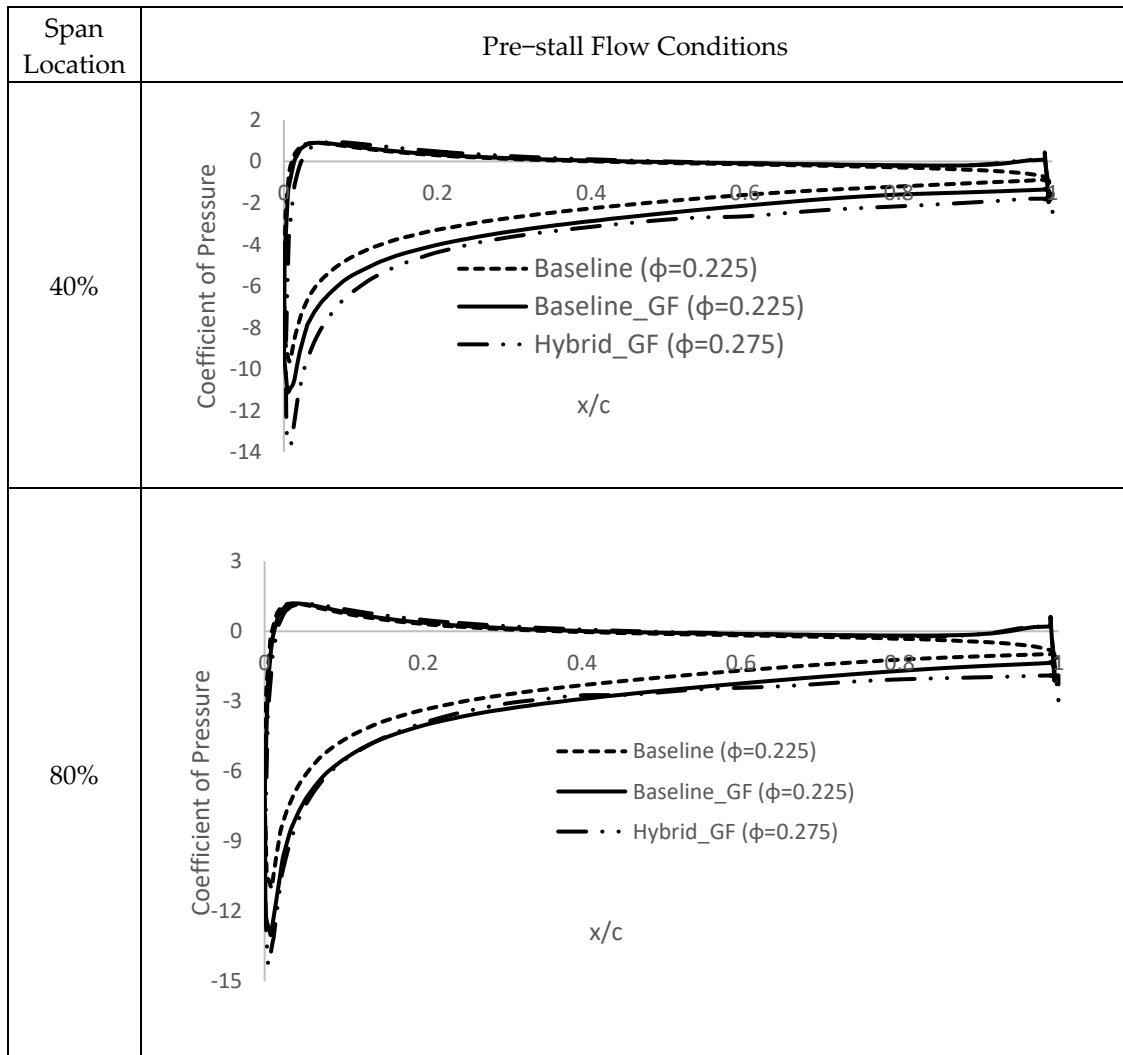| Span Location	Stall Flow Conditions
10%	
40%	
80%	

(**b**)

Figure 15. Wall shear in the X-direction at different span locations for (**a**) pre–stall; (**b**) stall flow conditions.

At the 40% span under pre–stall conditions, the hybrid turbine blades with GF experience flow separation earlier than other designs; flow detaches, reattachment, and again separates near the TE. For instance, x/c = 0.84, 0.95, and 0.75 for baseline, baseline with GF, and hybrid with GF, respectively. Further, at the 80% span, flow on the baseline and baseline with GF almost remain attached to the blade surface. However, the hybrid turbine with GF is exposed to high-pressure gradients and detaches early (x/c = 0.24).

Under stall conditions, at the 10% span, the hybrid turbine with GF suffers from flow recirculation and early separation than others. However, at the 40% and 80% span, the wall shear stress mostly remained zero along the chord lengths for all three turbine designs.

Figure 16 presents a comparison of blade loading at pre–stall and stall flow conditions for three turbines, focusing on the 40% and 80% span locations. The results reveal that, for all cases, the pressure distribution on the PS is similar for the turbines equipped with GF, while the baseline turbine shows slightly different pressure fields near the TE. Furthermore, under pre–stall conditions at the 40% span, the baseline turbine exhibits the highest suction pressure, followed by the baseline turbine equipped with GF and then the hybrid turbine with GF. However, the highest pressure drop is observed for the baseline with GF, producing the highest torque among other turbine designs prior to stall.
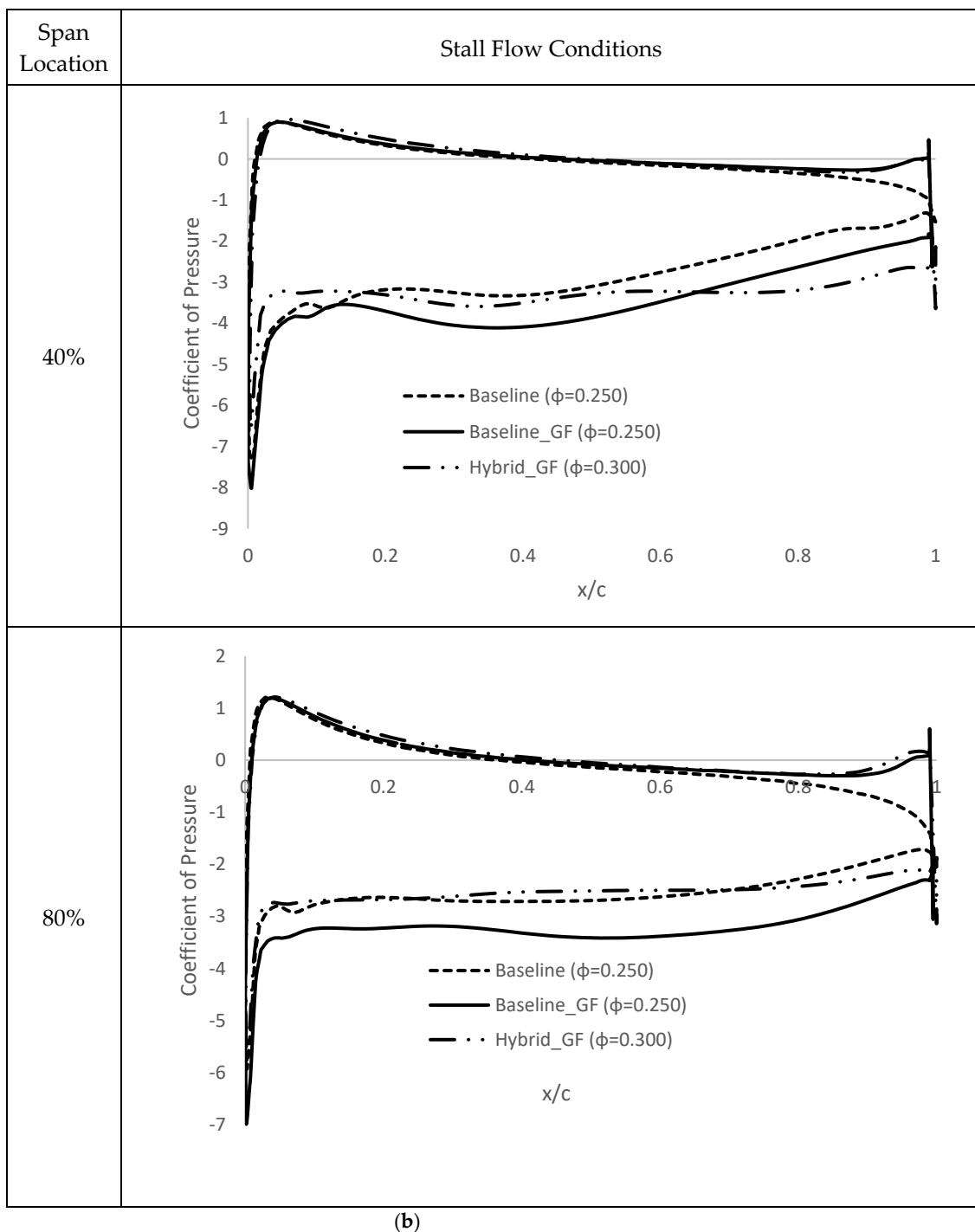

(**a**)

Figure 16. *Cont.*

Span Location	Stall Flow Conditions
40%	
80%	

(**b**)

Figure 16. Blade loading curve at different span locations for (**a**) pre–stall; (**b**) stall flow conditions.

4. Discussion

From the literature, it is evident that GF, the passive flow control mechanism, increases torque and power generation, while hybrid airfoil turbines can improve the operating range. However, no previous studies previously looked at GF and hybrid airfoils, both at the same time. Therefore, in the present study, we integrated a rectangular GF (flap height = 1.5%c, flap width = 0.5%c) adapted from reference [20] into the TE of a Wells turbine consisting of hybrid airfoil (NACA 0015 and NACA 0025) blades with variable chord distribution along the span. The current work assessed the aerodynamic performance of the hybrid turbine with GF compared to a turbine with a constant chord. In addition, a thorough analysis of the complex flow field surrounding the turbine blades was also conducted.

The hybrid turbine comprising NACA 0015 and NACA 0025 airfoils was considered over a constant thickness baseline design since the NACA0015 airfoil produces higher lift but stalls earlier, leading to a narrower operating range than the NACA0025 airfoil for a given Reynolds number [45]. Accordingly, a combination of both airfoils was selected to take advantage of the high lift and extended operating range that is highly desirable in wave energy harvesting.

Furthermore, to address the effect of centrifugal forces on the blade section at the hub and to improve its self-starting characteristics, a thicker blade profile (NACA 0025) is utilized at the hub. However, a thinner profile (NACA 0015) was selected for the tip to enable the optimal airfoil thickness ratio in the maximum axial velocity region near the hub.

Considering the limitations of computational resources and the required level of accuracy, we have chosen to use the RANS method for our simulations over LES or DNS. RANS modeling produces accurate results within the unstalled flow regimes; however, they are often inaccurate past the blade stall point. Refer to [46] for further information. For flows where the turbulence is not very strong, and the boundary layer is fully developed, the RANS k-ω SST model has been observed to offer improved precision. In these scenarios, LES and DNS may not be essential as the smaller turbulent structures they capture might not have a significant impact on the flow.

The results showed that the inclusion of GF improved the torque coefficient by 18.6% and 47.3% for the baseline and hybrid turbines, respectively. However, this came at the expense of a reduction in the peak efficiency of 8.5% and 7.4% for the two turbines, respectively. Furthermore, the hybrid turbine with GF delayed the onset of the stall by approximately 3° AOA.

The impact of GF on the aerodynamics of the turbine can be attributed to its ability to induce vortices that generate a pressure difference between the upper and lower surfaces of the blade, thereby increasing lift and delaying stall. However, this increase in lift is accompanied by an increase in drag, leading to a reduction in efficiency. Therefore, the optimal use of GF requires a trade-off between the increased lift and drag induced by the flap and the resulting impact on turbine efficiency.

5. Conclusions and Future Works

The incorporation of a rectangular Gurney flap at the trailing edge of a Wells turbine with hybrid airfoil blades can improve the aerodynamic performance of the turbine by increasing the torque coefficient and delaying the onset of stall. However, this also results in a reduction in peak efficiency. These findings could be useful in enhancing the power output of oscillating water column systems and making them more efficient.

There is still scope for further research in this area. Future works could investigate the use of different flap shapes and sizes to optimize the performance of the turbine. Moreover, the impact of varying the angle of attack and wave conditions on the turbine's performance could be investigated. Additionally, experimental validation of the numerical results could be conducted to validate the accuracy of the simulation. Such studies could contribute to improving the efficiency and reliability of wave energy conversion systems. Overall, the results of this study provide a promising approach to enhance the performance of Wells turbines, which could lead to significant advancements in wave energy harvesting technology.

Data Availability Statement: Not applicable.

Conflicts of Interest: The authors declare no conflict of interest.

Nomenclature

c	chord length (m)
C_T	torque coefficient
D	drag force (N)
F_x	axial force (N)
F_u	tangential force (N)
g	gravitational acceleration (m/s^2)
I	turbulence intensity
k	turbulence kinetic energy (m^2/s^2)
l	turbulent length scale (m)
L	lift force (N)
ΔP_0	static pressure drop (Pa)
ΔP_0^*	pressure drop coefficient
P_∞	free-stream static pressure (Pa)
Q	volumetric flow rate (m^3/s)
R	rotor radius (m)
Re	Reynolds number
T	blade torque (Nm)
U	mean flow velocity (m/s)
u_t	friction velocity (m/s)
U_{tip}	circumferential velocity at the blade tip (m/s)
v	axial velocity (m/s)
v_∞	free-stream axial velocity (m/s)
y	first layer distance from the wall (m)
y^+	dimensionless wall distance
ν_t	turbulent viscosity (kg/m^{-s})
ϕ	flow coefficient
η	efficiency
μ	dynamic viscosity (Ns/m^2)
ρ	air density (kg/m^3)
ρ_∞	free-stream air density (kg/m^3)
σ	blade solidity
ω	angular velocity (rad/s)
ν	kinematic viscosity (m^2/s)

References

1. Marco, T.; Pranzo, D.; Camporeale, S.; Pascazio, G. Improved Design of High Solidity Wells Turbine. In Proceedings of the Ninth European Wave and Tidal Energy Conference (EWTEC2011), Southampton, UK, 5–9 September 2011.
2. Uddin, M.N.; Atkinson, M.; Opoku, F. A Computational Fluid Dynamics Investigation of a Numerically Simulated Wave Tank. *Am. J. Mech. Eng.* **2020**, *8*, 40–49.
3. Opoku, F.; Uddin, M.N.; Atkinson, M. A Review of Computational Methods for Studying Oscillating Water Columns—The Navier-Stokes Based Equation Approach. *Renew. Sustain. Energy Rev.* **2023**, *174*, 113124. [CrossRef]
4. Starzmann, R.; Carolus, T.h. Effect of Blade Skew Strategies on the Operating Range and Aeroacoustic Performance of the Wells Turbine. *J. Turbomach.* **2013**, *136*, 11003. [CrossRef]
5. Curran, R.; Gato, L.M.C. The Energy Conversion Performance of Several Types of Wells Turbine Designs. *Proc. Inst. Mech. Eng. Part A J. Power Energy* **1997**, *211*, 133–145. [CrossRef]
6. Gato, L.M.C.; Warfield, V.; Thakker, A. Performance of a High-Solidity Wells Turbine for an OWC Wave Power Plant. *J. Energy Resour. Technol.* **1996**, *118*, 263–268. [CrossRef]
7. Thakker, A.; Dhanasekaran, T.S.; Ryan, J. Experimental Studies on Effect of Guide Vane Shape on Performance of Impulse Turbine for Wave Energy Conversion. *Renew. Energy* **2005**, *30*, 2203–2219. [CrossRef]

8. Thakker, A.; Dhanasekaran, T.S. Experimental and Computational Analysis on Guide Vane Losses of Impulse Turbine for Wave Energy Conversion. *Renew. Energy* **2005**, *30*, 1359–1372. [CrossRef]

9. Watterson, J.K.; Gillan, M.A.; Raghunathan, S.; Mitchell, R.D. Applications of Computational Fluid Dynamics to a Wave Energy Conversion Device. In Proceedings of the Thirty-Second Intersociety Energy Conversion Engineering Conference (Cat. No.97CH6203), Honolulu, HI, USA, 27 July–1 August 1997; Volume 3, pp. 1976–1981.

10. Taha, Z.; Sugiyono Sawada, T. A Comparison of Computational and Experimental Results of Wells Turbine Performance for Wave Energy Conversion. *Appl. Ocean. Res.* **2010**, *32*, 83–90. [CrossRef]

11. Takao, M.; Setoguchi, T.; Kinoue, Y.; Kaneko, K. Wells Turbine with End Plates for Wave Energy Conversion. *Ocean. Eng.* **2007**, *34*, 1790–1795. [CrossRef]

12. Soo, H.B.; Seung, M.J.; Won, H.S.; Sup, K.K. Aerodynamic Characteristics of Impulse Turbine with an End Plate for Wave Energy Conversion. *J. Ocean. Eng. Technol.* **2005**, *19*, 1–7.

13. M'zoughi, F.; Garrido, I.; Garrido, A.J.; De La Sen, M. Self-Adaptive Global-Best Harmony Search Algorithm-Based Airflow Control of a Wells-Turbine-Based Oscillating-Water Column. *Appl. Sci.* **2020**, *10*, 4628. [CrossRef]

14. Ormaza, M.A.; Goitia, M.A.; Hernández, A.J.G.; Hernández, I.G. Neural Control of the Wells Turbine-Generator Module. In Proceedings of the 48h IEEE Conference on Decision and Control (CDC) Held Jointly with 2009 28th Chinese Control Conference, Shanghai, China, 15–18 December 2009; pp. 7315–7320.

15. Muktadir, M.; Yi, S. Machine Vision-Based Detection of Surface Defects of 3D-Printed Objects. In Proceedings of the 2021 ASEE Virtual Annual Conference Content Access, Virtual, 19–26 July 2021.

16. Garfo, S.; Muktadir, M.; Yi, S. Defect Detection on 3D Print Products and in Concrete Structures Using Image Processing and Convolution Neural Network. *J. Mechatron. Robot.* **2020**, *4*, 74–84. [CrossRef]

17. Kumar, A.; Das, T.K.; Samad, A. Effect of Blade Skew, Endplate and Casing Groove on the Aerodynamic Performance of Wells Turbine for OWC: A Review. *J. Phys. Conf. Ser.* **2022**, *2217*, 012070. [CrossRef]

18. Gato, L.M.C.; Webster, M. An Experimental Investigation into the Effect of Rotor Blade Sweep on the Performance of the Variable-Pitch Wells Turbine. *Proc. Inst. Mech. Eng. Part A J. Power Energy* **2001**, *215*, 611–622. [CrossRef]

19. Graham, M.; Muradian, A.; Traub, L.W. Experimental Study on the Effect of Gurney Flap Thickness on Airfoil Performance. *J. Aircr.* **2018**, *55*, 897–904. [CrossRef]

20. Kotb, A.T.; Nawar, M.A.; Maksoud, R.M.A.E. The Effect of Rectangulargurney Flap on Wells Turbine Performance. *IOP Conf. Ser. Mater. Sci. Eng.* **2020**, *973*, 012006. [CrossRef]

21. Kotb, A.T.M.; Nawar, M.A.A.; Abd El Maksoud, R.M.; Mohamed, M.H. Comprehensive and Synergistic Analysis of Geometry Effect on an Axial Turbine Performance for Wave Energy Conversion. *Ocean. Eng.* **2021**, *233*, 109212. [CrossRef]

22. Kumar, P.M.; Samad, A. Introducing Gurney Flap to Wells Turbine Blade and Performance Analysis with OpenFOAM. *Ocean. Eng.* **2019**, *187*, 106212. [CrossRef]

23. Kotb, A.T.M.; Nawar, M.A.A.; El Maksoud, R.A.; Attai, Y.A.; Mohamed, M.H. Potential of Performance Improvement of a Modified Wells Turbine Using Passive Control for Wave Energy Conversion. *Ocean. Eng.* **2021**, *242*, 110178. [CrossRef]

24. Raghunathan, S.; Tan, C.P. Effect of Blade Profile on the Performance of the Wells Self-Rectifying Air Turbine. *Int. J. Heat Fluid Flow* **1985**, *6*, 17–22. [CrossRef]

25. Webster, M.; Gat, L.M.C. The Effect of Rotor Blade Shape On the Performance of the Wells Turbine. *Int. J. Offshore Polar Eng.* **2001**, *11*.

26. Shehata, A.S.; Xiao, Q.; Saqr, K.M.; Alexander, D. Wells Turbine for Wave Energy Conversion: A Review. *Int. J. Energy Res.* **2017**, *41*, 6–38. [CrossRef]

27. Shehata, A.S.; Saqr, K.M.; Shehadeh, M.; Xiao, Q.; Day, A.H. Entropy Generation Due to Viscous Dissipation around a Wells Turbine Blade: A Preliminary Numerical Study. *Energy Procedia* **2014**, *50*, 808–816. [CrossRef]

28. Shehata, A.S.; Saqr, K.M.; Xiao, Q.; Shehadeh, M.F.; Day, A. Performance Analysis of Wells Turbine Blades Using the Entropy Generation Minimization Method. *Renew. Energy* **2016**, *86*, 1123–1133. [CrossRef]

29. Soltanmohamadi, R.; Lakzian, E. Improved Design of Wells Turbine for Wave Energy Conversion Using Entropy Generation. *Meccanica* **2016**, *51*, 1713–1722. [CrossRef]

30. Suzuki, M.; Arakawa, C. Influence of Blade Profiles on Flow around Wells Turbine. *Int. J. Fluid Mach. Syst.* **2008**, *1*, 148–154. [CrossRef]

31. Takao, M.; Thakker, A.; Abdulhadi, R.; Setoguchi, T. Effect of Blade Profile on the Performance of a Large-Scale Wells Turbine for Wave-Energy Conversion. *Int. J. Sustain. Energy* **2006**, *25*, 53–61. [CrossRef]

32. Takao, M.; Takasaki, K.; Okuhara, S.; Setoguchi, T. Wells Turbine for Wave Energy Conversion—Improvement of Stall Characteristics by the Use of 3-Dimensional Blades. *J. Fluid Sci. Technol.* **2014**, *9*, JFST0052. [CrossRef]

33. Uddin, M.N.; Atkinson, M.; Das, T.K.; Esau, S. Computational Fluid Dynamics Investigation of a Novel Bi-Directional Axial Flow Turbine for Wave Energy Conversion. In *American Society of Mechanical Engineers Digital Collection*; American Society of Mechanical Engineering (ASME): New York, NY, USA, 2022.

34. Uddin, M.N.; Atkinson, M.D.; Opoku, F. Numerical Investigation of a Modified Denniss-Auld Turbine. In *AIAA AVIATION 2022 Forum*; American Institute of Aeronautics and Astronautics: Reston, VA, USA, 2022.

35. Opoku, F.; Atkinson, M.D.; Uddin, M.N. Computational Fluid Dynamics Investigation of a Novel Oscillating Water Column. In *AIAA SCITECH 2022 Forum*; American Institute of Aeronautics and Astronautics: Reston, VA, USA, 2022.

36. Opoku, F.; Atkinson, M.; Uddin, M.N. Numerical Investigation of an Offshore Oscillating Water Column. *Am. J. Mech. Eng.* **2020**, *8*, 88–105.

37. Karim, S.M.S.; Lin, Y.-L.; Kaplan, M.L. Formation Mechanisms of the Mesoscale Environment Conducive to a Downslope Windstorm over the Cuyamaca Mountains Associated with Santa Ana Wind during the Cedar Fire (2003). *J. Appl. Meteorol. Climatol.* **2022**, *61*, 1797–1818. [CrossRef]

38. Ferguson, F.; Feng, D.; Gao, Y. Investigating the Flowfield Physics Within Compressible Turbulent Boundary Layers. In *American Society of Mechanical Engineers Digital Collection*; American Society of Mechanical Engineering (ASME): New York, NY, USA, 2020.

39. Das, T.K.; Samad, A. Influence of Stall Fences on the Performance of Wells Turbine. *Energy* **2020**, *194*, 116864. [CrossRef]

40. Shaaban, S. Aero-Economical Optimization of Wells Turbine Rotor Geometry. *Energy Convers. Manag.* **2016**, *126*, 20–31. [CrossRef]

41. Alkhalifa, A.S.; Uddin, M.N.; Atkinson, M. Aerodynamic Performance Analysis of Trailing Edge Serrations on a Wells Turbine. *Energies* **2022**, *15*, 9075. [CrossRef]

42. Roache, P.J. Verification of Codes and Calculations. *AIAA J.* **1998**, *36*, 696–702. [CrossRef]

43. Samad, A.; Samad, A. Nature-Inspired Design of a Turbine Blade Harnessing Wave Energy. *Proc. Inst. Mech. Eng. Part A J. Power Energy* **2018**, *234*, 670–689.

44. Manna, P.; Dharavath, M.; Sinha, P.K.; Chakraborty, D. Optimization of a Flight-Worthy Scramjet Combustor through CFD. *Aerosp. Sci. Technol.* **2013**, *27*, 138–146. [CrossRef]

45. Sheldahl, R.E.; Klimas, P.C. *Aerodynamic Characteristics of Seven Symmetrical Airfoil Sections through 180-Degree Angle of Attack for Use in Aerodynamic Analysis of Vertical Axis Wind Turbines*; SAND-80-2114; Sandia National Labs.: Albuquerque, NM, USA, 1981; p. 6548367.

46. Schobeiri, M.T.; Abdelfattah, S. On the Reliability of RANS and URANS Numerical Results for High-Pressure Turbine Simulations: A Benchmark Experimental and Numerical Study on Performance and Interstage Flow Behavior of High-Pressure Turbines at Design and Off-Design Conditions Using Two Different Turbine Designs. *J. Turbomach.* **2013**, *135*, 61012.